

Bioturbation, heavy mineral concentration, and high gamma-ray activity in the Lower Cretaceous McMurray Formation, Canada

Milovan Fustic ^{a,b,*}, Rajeev Nair ^b, Andreas Wetzel ^c, Raza Siddiqui ^b, William Matthews ^b, Raphael Wust ^d, Manuel Bringue ^e, Jagos Radovic ^b

^a *Nazarbayev University, School of Mining and Geosciences, Nursultan, Kazakhstan*

^b *University of Calgary, Calgary, Canada*

^c *University of Basel, Switzerland*

^d *James Cook University, Townsville, Australia*

^e *Geological Survey of Canada, Calgary, Canada*

Published 2021 in: *Palaeogeography, Palaeoclimatology, Palaeoecology* 564: 110187 (17 p.)

<https://doi.org/10.1016/j.palaeo.2020.110187>

* Corresponding author at: Nazarbayev University, School of Mining and Geosciences, Nursultan, Kazakhstan.

E-mail addresses: milovan.fustic@nu.edu.kz (M. Fustic), rnair@ucalgary.ca (R. Nair), andreas.wetzel@unibas.ch (A. Wetzel), wamatthe@ucalgary.ca (W. Matthews), raphael.wust@jcu.edu.au (R. Wust), manuel.bringue@canada.ca (M. Bringue), Jagos.Radovic@ucalgary.ca (J. Radovic).

Keywords: ichnology, zircon, biosphere, provenance, point bar

Abstract

In the Lower Cretaceous McMurray Formation (Alberta, Canada), many intervals of intensely bioturbated (Bioturbation Index = 5–6) fine-grained sediments are characterized by high gamma-ray (GR) readings. Several methods, including sedimentary facies analysis, thin-section petrography, handheld spectral gamma-ray, portable X-ray fluorescence, X-ray diffraction, inductively coupled plasma-mass spectrometry, microprobe of K-feldspar, energy dispersive spectroscopy, and detrital zircon geochronology by laser ablation-inductively coupled plasma-mass spectrometry, were used to investigate the interval of interest in core samples. The mineralogical analysis shows that these intervals are enriched in heavy mineral grains, and particularly in zircons. The content of radioactive elements is variable. Thorium is commonly elevated up to three times, uranium nil to two times, and potassium content usually remains normal. The studied intervals consist of interbedded, bitumen-saturated cross-bedded and/or ripple cross-laminated sandstone (high-energy deposits) and light-gray bioturbated mudstone (low-energy deposits), commonly addressed as inclined heterolithic strata (IHS). IHS represent tidally influenced, brackish-water, upper point-bar deposits. The zircon grains become concentrated while hydraulic processes interact with bioturbation: the burrowing animals cause significant sediment mixing that allows the lightest sediment particles to go back into the suspension. Additionally, bioturbation increases the surface roughness along the sediment-water interface and, causes more turbulent flow, allowing for quartz and other light grains to be removed by traction and/or saltation, while dispersed heavier zircon grains become trapped and concentrated in open burrows.

So far, this study is the first to demonstrate the importance of bioturbation in the enrichment of zircon grains in IHS. The interaction of bioturbation and hydraulic processes explains the apparently counter-intuitive enrichment of heavy minerals in a low-energy depositional setting. This scenario likely applies to numerous intervals characterized by similar GR and/or zirconium spikes across the McMurray Formation. Furthermore, it can be expected that in other sedimentary basins and stratigraphic units, similar studies will demonstrate that the proposed mechanism is universal.

1. Introduction

Petrophysical rock and fluid property estimates from the measurements of gamma-ray (GR) emission, electrical conductivity/resistivity, hydrogen content (neutron), density, and velocity are commonly used to characterize, interpret, and evaluate subsurface stratigraphy, sedimentology, and petroleum resources. These measurements are most commonly conducted immediately after drilling, under open-hole conditions, which allows direct contact of logging tools with rocks and fluids. GR measurements record the total emissions of uranium (U), thorium (Th), and potassium (K) – the most abundant sources of GR in sedimentary systems. GR logs are typically used for reservoir characterization, and radiation sources are commonly inferred from the knowledge about depositional settings. However, the determination of point sources of radiation in specific lithologies is warranted in many situations, particularly where unusual GR signatures are present.

Bioturbation is the process of sediment reworking by animals or plants via burrowing, ingestion, and/or defecation during or shortly after deposition. It can significantly modify primary depositional features, including sedimentary structures and/or grain and mineral distributions. The percentage of original fabric reworked by biogenic activity is commonly estimated using the “Bioturbation Index” approach (BI; Taylor and Goldring, 1993). BI is a quantitative estimate of burrow density, amount of burrow overlap, and the sharpness of the original sedimentary fabric. It is represented on a scale of 0 to 6, where 0 represents the absence of burrows, and 6 indicates complete bioturbation with no original sedimentary structures preserved (Reineck, 1963; Reineck and Singh, 1980; Taylor and Goldring, 1993). Biogenic sedimentary structures resulting from bioturbation provide valuable information about biota, water depth, salinity, turbidity, and energy during sediment deposition. This information, coupled with data from physical sedimentary structures, may allow the interpretation of depositional environments (e.g., Reineck and Singh, 1980; Seilacher, 1967). Many studies have documented the impact of bioturbation on porosity and permeability (Spila et al., 2009; Tonkin et al., 2010; Gingras et al., 2012; La Croix et al., 2012), but there is a paucity of evidence documenting specific mineral sorting patterns related to bioturbation. In this study, we show a possible link between bioturbation and concentration of heavy minerals with GR-generating potential.

Herein, we investigated and described fine-grained sediment from the Lower Cretaceous McMurray Formation, Western Canada Sedimentary Basin (Figs. 1A, 2) characterized by anomalously high GR emissions and intense bioturbation (BI = 5–6; Fig. 3). To understand this phenomenon, the main objectives of this study were to identify the sources of radioactive anomalies recorded by GR logs, explain their origin in a geological (sedimentological) context, and decipher potential interdependencies of mineralogy, hydrodynamics, and bioturbation. Obtained multi-disciplinary data and proposed novel concept of enrichment of heavy mineral grains by bioturbation add on to previous studies on the interpretation of depositional environments.

2. Geological setting

The Athabasca Oil Sands Deposit (AOSD) is located in northeastern Alberta, Canada (Fig. 1A). AOSD hosts the largest natural bitumen (severely degraded oil) deposits in the world, with an estimated initial oil-in-place of 1.7 trillion barrels (Alberta Energy Regulator, 2015). The primary bitumen-bearing units are the clastic deposits of the Lower Cretaceous McMurray Formation (Fig. 2).

The McMurray Formation sediments were deposited in the eastern portion of the Cordilleran foreland basin along the southern margin of the Western Interior Seaway during the late Barremian and Aptian (Hein et al., 2013). The initial accommodation space was likely formed prior to the formation of the foreland basin by regional salt-dissolution, which resulted in the partial collapse of the overlying strata (e.g., Broughton, 2016) and/or differential erosion of the underlying Devonian strata by northward-flowing rivers (Hubbard et al., 2016). These processes formed a very irregular sub-Cretaceous unconformity, marking the base of the McMurray Formation (Fig. 2). The McMurray Formation is known for its complex internal stratigraphy formed by the interplay of fluctuating sediment supply, drainage system dynamics, and relative sea-level changes within the low-accommodation sedimentary basin setting (Hein and Cotterill, 2006; Flach et al., 2020). The McMurray Formation is informally subdivided into the lower (continental), middle (open estuarine and estuarine channel complexes), and

upper (marine) members (Carrigy, 1959; Fig. 2). The formation of multiple inter-fingering valleys within the middle member (Fig. 2) is attributed to high-frequency sea-level changes (Ranger and Pemberton, 1997; Martin, 2018; Horner et al., 2019) or high-frequency avulsions of meander belts occurring during a continuous sea-level rise (Flach et al., 2020).

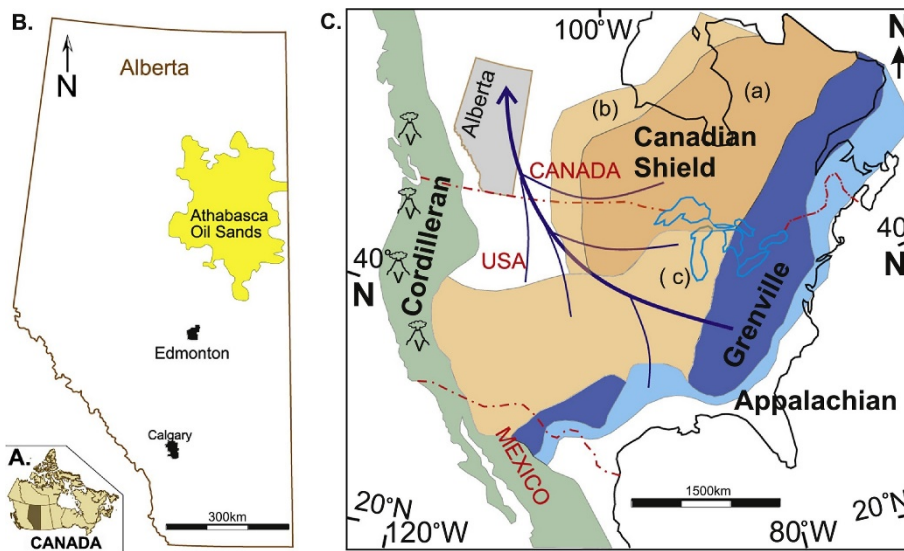


Fig. 1. Geographic location of the Athabasca Oil Sands area within Alberta, Canada (A–B) and interpretation of the Precambrian and Phanerozoic age sediment sources by Benyon et al. (2014) and (Dickinson and Gehrels, 2009) (C), where (a) represents the Superior Province of the Canadian Shield (~2.5 Ga); (b) represents the Trans-Hudson Province (~1.8 Ga); and (c) represents other ca. 1.8 Ga old provinces. Key: dark blue lines refer to the trans-continental paleo-drainage system during the Cretaceous; “v” demarcate Mesozoic volcanoes of the Cordilleran magmatic arc (modified after Benyon et al., 2014).

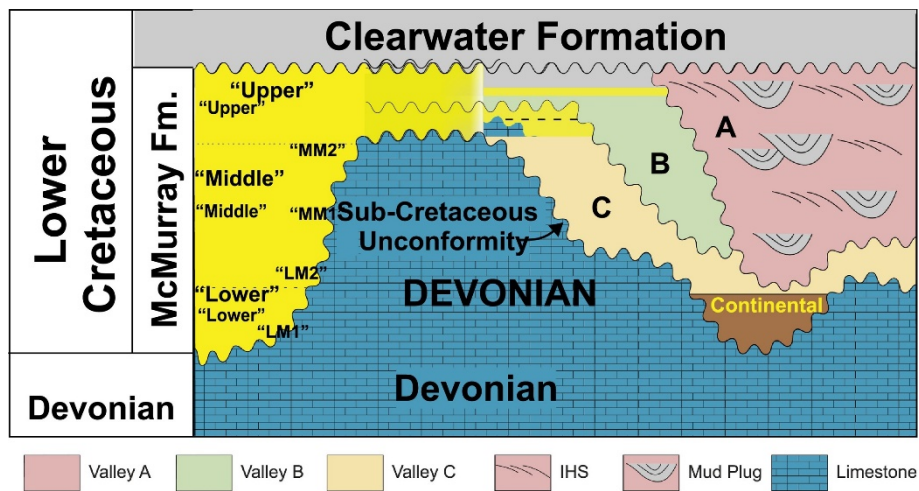


Fig. 2. Schematic stratigraphic framework of northeastern Alberta, including the informal subdivision of the McMurray Formation into the lower, middle, and upper members (Carrigy, 1959). On the right, an alternative interpretation based on the incised-valley system (Fustic et al., 2013b based on principles proposed by Wightman and Pemberton, 1997; Hein et al., 2000, 2001; Hein and Cotterill, 2006; Ranger and Pemberton, 1997) formed in response to relative sea-level changes. Valley C is the oldest, and Valley A is the youngest, implying that the latter erodes sediments of both Valleys B and C. Large-scale depositional elements with their dominant lithologies and architecture are demarcated in Valley A. Note multiple stacked channel deposits within Valley A. IHS – inclined heterolithic strata. Modified after Fustic et al. (2013b).

This study focuses on multiple stacked and inter-fingering, large-scale (up to 40-m-thick) meandering river deposits, which belong to the multiple “valleys” of the middle member of the McMurray Formation (Hubbard et al., 2011; Musial et al., 2012; Fustic et al., 2012; Fig. 2). Diagnostic features of these meandering deposits are the inclined heterolithic strata (IHS; *sensu* Thomas et al., 1987) interpreted as a product of lateral and/or downstream accretion of point bars (Smith et al., 2009; Hubbard et al., 2011;

Fustic et al., 2012; Ghinassi et al., 2016). IHS is dominated by brackish-water trace fossils, whereas *Skolithos* and *Cylindrichnus* indicate tidal influence (Pemberton et al., 1982; Ranger and Pemberton, 1992; Ranger and Pemberton, 1997; Hubbard et al., 2011; Jablonski and Dalrymple, 2016; Gingras et al., 2016; Shchepetkina et al., 2017).

The variable intensity of bioturbation coupled with the low diversity of ichnogenera in the McMurray Formation point-bar deposits is generally caused by such environmental conditions as marked variations in river discharge, benthic food availability, turbidity, and salinity (Pemberton et al., 1982; Ranger and Pemberton, 1992; Ranger and Pemberton, 1997; Hubbard et al., 2011; Jablonski and Dalrymple, 2016; Gingras et al., 2016; Shchepetkina et al., 2017; Broughton, 2018).

Recent provenance studies using detrital zircon U–Pb geochronology have shown that the McMurray Formation sediments originated from the proximal Proterozoic and Archean rocks of the Canadian Shield and the distal rocks of the Grenville and Appalachian orogens (Fig. 1B). The continental-scale sediment transport must have taken place in trans-continental drainage systems (Benyon et al., 2014, 2016; Blum and Pecha, 2014; Fig. 1B). A recent analysis of a very thin bentonite lamina in a coal layer at the top of the Lower McMurray Formation (Rinke-Hardekopf et al., 2019) also suggests sporadic ashfalls sourced from the Cordilleran volcanic eruptions (Fig. 1B). Although kimberlites are known to have erupted through the Canadian Shield between 106 and 99 Ma (Kjarsgaard et al., 2006; White et al., 2007; Eccles, 2011), no eruptive material of that origin has been identified in the McMurray Formation yet.

Due to the AOSD reservoir complexity, a high density of vertical, “stratigraphic” wells is required to assess the hydrocarbon resource and optimize surface mining operations and well placement for in situ thermal recovery technologies. Consequently, tens of thousands of vertical wells have been drilled, cored, and logged to estimate the petrophysical properties of bitumen-bearing sediments and fluids in their pores. Based on the Alberta Energy Regulator (AER) regulations, subsurface data becomes publicly available after one year of confidentiality. GR logging is commonly used as the first method for a rapid interpretation of stratigraphy and depositional environments, as well as calculations of sand-mud and/or net-to-gross ratio. The predominance of quartz in the sand fraction and gamma-emitting potassium (K) in the clay fraction commonly proofed GR logs as reliable tools for interpreting lithological variations and depositional environments. Specifically, low GR (<60 API [API–American Petroleum Institute units]) represents clean quartz sands, moderate GR (60–90 API) indicates muddy sandstone or interbedded sandstone and mudstone, and high GR (90–120 API) specifies mudstone. Values greater than 120 API are very rare. Spectral GR techniques developed to distinguish the individual contributions of potassium (K), uranium (U), and thorium (Th) to total GR are rarely applied in open holes. Instead, in the cases of uncertain GR data, either high-resolution (i.e., every 0.05 m) spectral GR measurements using a handheld spectrometer (commonly referred to as scintillometer) or advanced continuous spectral GR recording on cores in the laboratory are done to resolve radiation sources and mineral composition.

In the McMurray Formation, elevated GR spikes are commonly caused by increased proportions of feldspar grains in quartz-dominated sandstone packages. This association is usually attributed to the occasional pulses of arkosic sand characterized by low compositional maturity and delivered from the Canadian Shield (Fig. 1B). GR spikes within the mudstone and fine-grained sandstone layers of the McMurray Formation have received less attention and are the focus of this study. Intervals with higher than expected natural radioactivity emissions are commonly referred to as “hot” GR zones. These zones are defined by: (i) the GR spike values exceeding the shale baseline (Fig. 3); (ii) evidence of high porosity from resistivity logs, indicating a porous oil-saturated interval; and (iii) relatively low shale volume (Vsh) calculated from density-neutron logs. High porosity inferred from resistivity logs contradicts the interpretation of high clay content typically ascribed to the GR intervals with high readings. The latter interpretation also explains the contradictory results in Vsh calculations from density neutron and GR logs.

3. Material and methods

GeoSCOUT (product of geoLOGIC Systems Inc.) was used to access the petrophysical log database and visually screen for intervals characterized by anomalously high gamma-ray values compared to the

shale baseline within individual wells. Depositional environments were interpreted based on core lithology, grain size, and physical and biogenic sedimentary structures (Figs. 3–6) as well as GR and other petrophysical logs (Figs. 3–6), including dipmeter, when available (Fig. 5). A dipmeter log is a powerful tool for defining vertical channel continuity in the McMurray Formation (Brekke and Evoy, 2004; Fustic, 2007; Brekke et al., 2017). The GR logs that contained spikes above the shale baseline were transferred to GEOLOG (product of Emerson E&P Software) for quantitative petrophysical analysis, such as the calculation of shale volume from GR and neutron-density logs. The study was limited to the cores available at the Alberta Energy Regulator’s (AER) Core Storage Facility. The AER core analysis database revealed the availability of various datasets, including X-ray fluorescence (XRF), for some wells (Figs. 4–6).

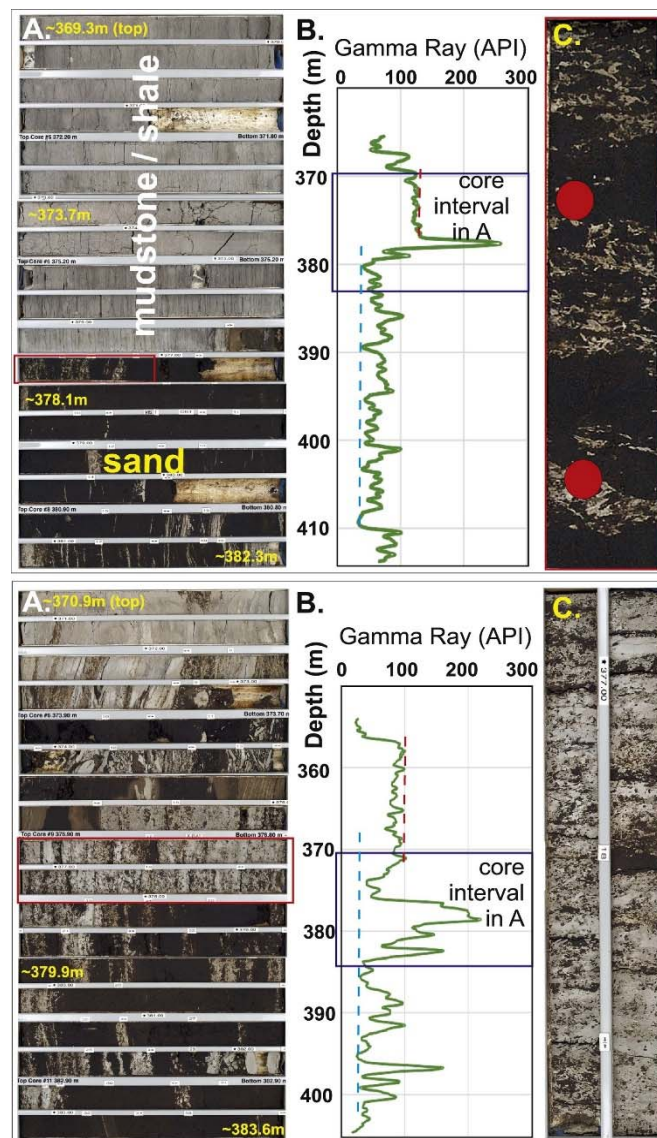


Fig. 3. Well 1 (1AA 01-12-076-07 W4M [top]) and Well X (1AA 12-12-076-07 W4M [bottom]). Typical examples of "hot" (anomalously high) GR intervals associated with intensely bioturbated beds. A) Core images. Sand is black due to heavy oil (bitumen) saturation. Mudstone is light-gray. The red boxes indicate the close-up of the interval of interest in (C). B) Total GR logs. The GR shale line (red dashed line) in both wells ranges between 100 and 120 API, while the GR peaks in the bioturbated zones constitute 270 and 220 API in Wells 2 and X, respectively. The blue dashed line is the sand line. C) Close-up view of the interval of interest. Red dots show ICP-MS spots (Table 3). Note: Well 1 was sampled and studied, while permission to sample well X was not obtained. (For interpretation of the references to colour in this figure legend, the reader is referred to the web version of this article.)

Strict government regulations on destructive core analysis for the preparation of thin sections, Inductively Coupled Plasma Mass Spectrometry (ICP-MS) geochemistry, and zircon geochronology (high volume of sediments required) limited the investigations. For this research, special sampling

permission was given only for a short (~0.3 m; Fig. 5) core interval in well A (1AA 09-02-081-09 W4M; lat 55°59'36.72" N, long 111°17'16.23" W; Fig. 5). A "hot" GR interval in that well was identified based on a significant separation of shale volume curves calculated from GR and neutron-density (Fig. 5). Limited destructive analysis was also permitted for selected intervals in well 1 (1AA 01-12-076-07 W4M; lat 55°32'59.85" N, long 110°57'59.40" W, Fig. 3A), well 2 (1AA 03-12-076-07 W4M; lat 55°33'52.18" N, long 110°57'12.24" W; Fig. 5), and well 3 (1AA 14-14-076-07 W4M; lat 55°35'23.93" N, long 110°58'45.41" W; Fig. 6). Well X (1AA 121,207,607 W4M; lat 55°34'16.43" N, long 110°57'41.13"; Fig. 3B) was intended to be studied in more detail, but permission was not given. We kept it as an illustration of relationship between GR and bioturbation.

3.1. Analyses conducted on Well A

Facies analysis, spectral GR, and XRF measurements were conducted on an approximately 20-m-long slabbed core interval of well A (Fig. 5). For the facies analysis, the slabbed core surfaces were examined macroscopically and by hand lens. The grain size was estimated using a comparison chart, while the ichnological content was evaluated by identifying the biogenic sedimentary structures and intensity of bioturbation to estimate BI. Among the bioturbation structures, biodeformation structures display no distinct outlines that would allow classification in terms of paleontological nomenclature (Schäfer, 1956). In contrast, trace fossils display distinct outlines and exhibit typical burrow geometry. The trace fossils were identified on the ichnogenic level because only 2D surfaces were available for investigation. In particular, the morphological approach was used to identify trace-fossil taxa (Knaust, 2017).

The spectral GR measurements were obtained using a handheld spectrometer (RS-230 BGO, Radiation Solutions Inc.). These data provided the contributions of U, Th, and K to compare the sum with total radioactivity measured by an open-hole log. Each measurement was set to 90 s. A total of 33 measurements, or approximately one measurement every 0.25 m, were taken from a depth interval of 446.45 to 454.64 m (Table 1).

Table 1

Spectral gamma-ray analysis obtained using a handheld spectrometer (model RS-230 BGO).

Depth (m)	U[ppm]	Th[ppm]	K[wt%]
446.45	1.8	4.3	0.7
446.73	1.5	5.1	0.8
447.01	1.8	3.9	0.5
447.29	2.0	3.8	0.7
447.57	2.4	4.4	0.5
447.85	2.0	4.5	0.6
448.13	1.7	3.8	0.6
448.41	1.5	5.0	0.6
448.69	1.9	4.8	0.6
448.97	1.4	5.0	0.7
449.25	2.0	3.7	0.7
449.53	2.1	4.1	0.6
449.81	1.5	5.1	0.5
450.09	1.4	3.9	0.5
450.37	2.2	4.3	0.6
450.95	1.7	5.8	0.6
451.1	2.2	4.8	0.5
451.25	1.8	5.1	0.6
451.52	2.1	4.3	0.6
451.79	1.4	5.6	0.5
452.06	1.5	2.8	0.7
452.36	1.5	3.1	0.6
452.55	1.6	4.7	0.6
452.74	1.4	5.1	0.5
452.93	1.8	3.5	0.5
453.12	1.7	3.0	0.5
453.31	2.1	3.9	0.4
453.5	1.2	3.3	0.6
453.69	1.5	4.3	0.5
453.88	1.6	3.1	0.7
454.07	1.7	2.5	0.6
454.26	1.8	3.9	0.5
454.45	1.7	3.2	0.6
454.64	1.7	2.8	0.4
Average	1.7	4.1	0.6

XRF was conducted directly on the split core surface using a Bruker Tracer 5G with helium (He) purge in the He Geochem mode. Any surface contaminants were removed by gentle washing and light scraping, if necessary. The slabbed core was dried out before the XRF measurements. Twenty sample points from the interval of interest were measured and analyzed (Table 2, Fig. 5).

A number of specialized analyses were conducted on five samples collected from immediately below and above the interval characterized by increased GR emission, as inferred from Vsh GR and Vsh density separation (Fig. 5A) and intense bioturbation (Fig. 5B). The analyses included thin-section petrography, X-ray diffraction (XRD), electron microprobe analyses (EMPA), inductively coupled plasma-mass spectrometry (ICP-MS), and laser ablation-inductively coupled plasma-mass spectrometry (LA-ICP-MS) (Table 3; Fig. 5C). Thin-section preparation included the removal of bitumen with toluene (solvent), followed by an alcohol wash to remove salts, and impregnation with epoxy after drying. The samples were mounted onto a glass slide, where they were ground to a total thickness of 30 µm and then polished.

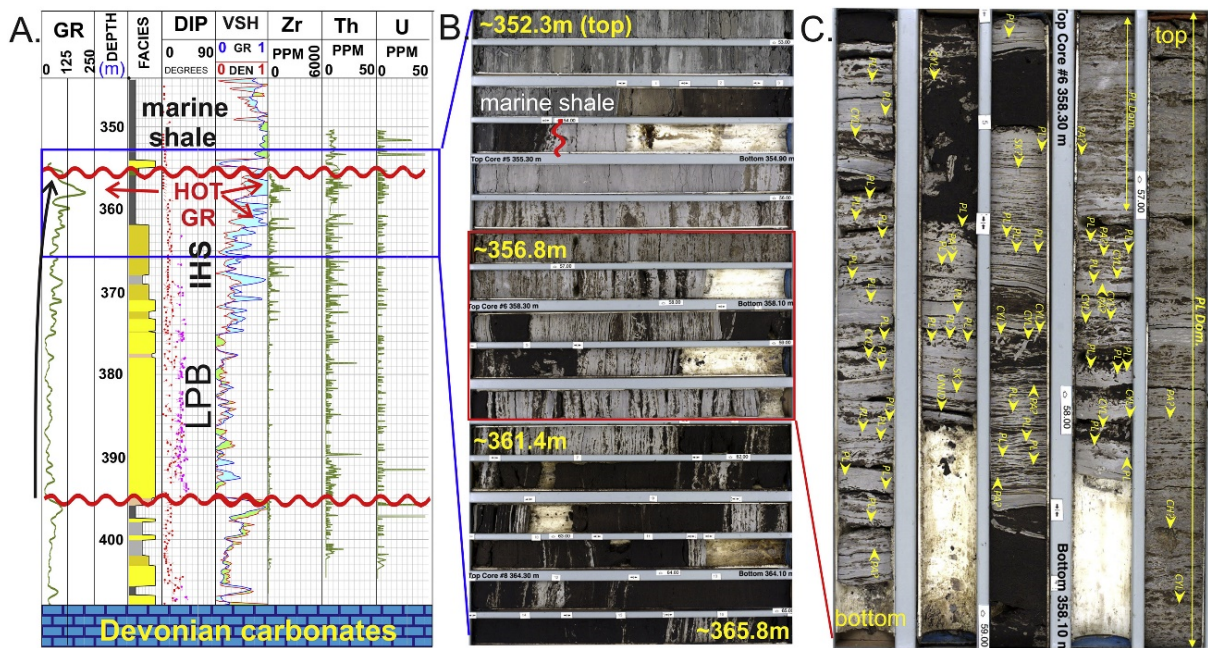


Fig. 4. Well 2 (1AA 03-12-076-07 W4M). A) Composite log and geochemical data (340–410 m). Composite log: GR – gamma-ray, DIP – dipmeter, VSH – volume shale, DEN – density porosity, Zr – zirconium, Th – thorium; U – uranium (in ppm from XRF). In facies column: yellow – clean sand; orange – sand-dominated IHS; light-gray – mud-dominated IHS; and dark-gray – mudstone. Wavy red lines show major erosional surfaces; straight red arrows show hot GR intervals; black curved arrow points to vertical continuity of a single, large-scale point bar. DIP column: red tad-poles show IHS dips, and purple tad-poles cross-bed dips; LPB – lower point bar. The blue rectangle indicates the core interval in (B). B) Core images of the “hot” GR interval (352.3–365.8 m) showing bitumen-saturated sandstone overlain by mudstone and the transition to marine shale. The red box demarcates the core interval in (C). C) Close-up view of the interval of interest with annotated trace fossils. The diminutive and restricted trace-fossil assemblage is dominated by Planolites (PL), moderate occurrences of *Cylindrichnus* (CYL), and minor *Palaeophycus* (PA) and *Skolithos* (SK).

Table 2
X-ray fluorescence data obtained by the analyses of core surface using a Bruker 5G XRF instrument.

Depth	Si	Al	Fe	K	Ca	Mg	S	Na	Cl	Rb	Sr	Zr	Mo	V	Mn	Ti	Cr	Ni	Cu	Zn	P	As	Y	Pb	Co	Ga	Se	Nb	Ba	
Wt%	Wt%	Wt%	Wt%	Wt%	Wt%	Wt%	Wt%	Wt%	Wt%	PPM	PPM	PPM	PPM	PPM	PPM	PPM	PPM	PPM	PPM	PPM	PPM	PPM	PPM	PPM	PPM	PPM	PPM	PPM		
446.45	34.87	7.84	0.81	1.36	0.15	0.28	0.38	0.47	0.06	75	171	457	2	36	61	4500	17	19	19	40	104	4	34	20	1	15	0	23	618	
446.47	33.71	7.07	0.77	1.28	0.18	0.25	0.41	0.56	0.06	73	161	503	1	52	42	4285	26	36	10	46	163	5	33	9	1	13	2	19	689	
448.85	28.61	4.54	0.76	0.74	0.25	0.00	1.67	0.59	0.48	23	27	915	0	38	229	3420	48	19	4	22	62	5	26	0	1	2	0	15	298	
448.87	28.04	4.78	1.07	0.78	0.26	0.04	0.90	6.07	5.75	51	93	733	0	26	289	4202	19	22	13	37	90	5	41	8	1	8	2	22	421	
449.15	30.11	6.74	2.88	1.03	0.40	0.33	1.01	1.90	1.26	47	92	384	4	56	1193	3911	15	28	11	54	198	5	28	11	9	11	0	18	468	
449.17	33.04	6.23	1.72	1.11	0.36	0.29	0.80	1.49	0.72	51	101	398	4	45	624	4142	0	24	13	39	102	6	27	7	3	10	0	19	410	
449.45	32.93	5.88	0.97	0.99	0.26	0.14	0.81	0.52	0.16	48	79	386	7	44	370	3167	16	21	9	42	93	5	22	8	1	8	0	15	580	
449.47	32.33	4.57	0.71	0.74	0.26	0.00	1.15	0.62	5.71	41	73	361	1	14	209	2909	49	22	12	30	0	5	21	10	1	6	0	11	403	
449.75	33.36	6.64	1.02	1.12	0.27	0.22	0.40	2.32	1.41	57	116	562	4	22	303	4305	27	19	9	41	197	7	32	12	1	11	0	18	499	
449.77	28.63	5.03	0.72	0.79	0.27	0.08	0.50	6.74	6.30	42	78	701	2	52	210	3196	27	19	13	33	32	5	30	15	1	9	2	20	488	
450.05	20.88	3.39	0.66	0.53	0.25	0.00	0.45	12.54	12.45	49	97	518	2	21	170	2341	38	12	10	36	60	6	28	14	1	8	3	19	444	
450.07	27.44	4.32	0.55	0.71	0.29	0.00	0.58	7.72	8.10	41	80	306	2	0	132	2726	28	10	9	31	0	5	17	17	0	6	0	15	327	
450.35	32.80	2.66	0.16	0.54	0.17	0.00	0.99	0.49	0.12	19	23	208	5	50	33	1057	31	3	0	15	227	5	9	13	0	3	0	8	182	
450.37	34.39	2.49	0.19	0.42	0.17	0.00	0.77	0.35	0.08	10	19	902	3	26	31	2004	22	3	5	16	297	4	15	0	0	2	0	13	239	
450.65	31.44	2.85	0.23	0.51	0.22	0.00	2.09	0.53	0.33	16	43	392	0	36	19	2285	0	9	3	19	219	7	13	9	0	4	0	6	207	
450.67	33.55	2.66	0.17	0.52	0.14	0.00	1.25	0.62	0.24	18	29	359	0	0	33	1511	0	9	0	11	131	3	18	10	0	2	0	8	392	
450.95	32.41	2.25	0.21	0.41	0.18	0.00	1.53	0.55	0.17	11	19	4849	0	12	56	3239	25	7	17	11	1891	7	100	0	0	6	0	2	18	216
450.97	30.69	2.09	0.20	0.41	0.13	0.00	0.89	0.43	0.21	8	20	1743	0	0	72	2698	118	10	9	13	355	7	41	8	0	2	2	18	146	
451.10	30.00	2.85	0.28	0.56	0.31	0.00	3.50	0.89	1.02	20	69	259	4	67	31	3242	19	14	6	19	259	7	12	10	0	5	0	4	421	
451.12	32.79	2.14	0.14	0.48	0.17	0.00	2.34	1.24	0.91	15	18	185	2	31	25	1423	0	9	3	15	105	4	11	0	0	0	0	4	309	
451.25	25.71	2.01	0.22	0.47	0.13	0.00	1.45	6.95	7.14	24	37	126	4	27	23	1198	0	14	7	17	0	2	6	7	0	5	0	5	415	
451.27	25.58	3.40	0.46	0.59	0.24	0.00	1.13	9.71	8.85	44	80	1339	0	51	40	2961	0	17	9	26	247	6	39	9	0	6	0	18	533	
451.52	30.19	4.25	0.33	0.67	0.15	0.00	0.90	2.59	2.71	29	46	266	4	16	42	2195	0	22	25	24	65	4	14	0	0	5	0	9	419	
451.54	28.24	4.29	0.56	0.79	0.26	0.04	0.69	7.37	4.96	56	102	1478	5	59	69	2937	38	22	36	34	152	4	42	13	1	7	0	20	448	
451.79	31.39	3.54	0.34	0.68	0.25	0.05	1.63	0.46	0.15	23	33	336	2	47	40	2002	0	19	22	15	47	4	16	0	0	3	0	10	354	
451.81	34.28	4.33	0.42	0.77	0.21	0.04	1.05	0.33	0.16	33	60	1496	2	17	43	2466	49	17	27	20	127	7	39	0	0	6	0	14	468	
452.06	31.81	2.27	0.15	0.68	0.18	0.00	1.57	0.49	0.13	26	33	168	0	26	24	931	13	10	0	10	107	3	3	20	0	0	0	4	315	
452.08	31.95	3.38	0.26	0.68	0.21	0.00	2.01	0.47	0.28	28	44	119	1	13	30	1232	15	14	0	17	0	2	7	9	0	3	0	3	423	
452.36	29.92	1.74	0.12	0.55	0.17	0.00	1.06	0.45	0.18	19	26	62	0	35	15	568	0	9	8	14	261	5	6	12	0	0	0	0	200	
452.38	29.85	2.61	0.20	0.53	0.25	0.00	1.58	0.93	0.30	18	30	95	4	38	23	1590	0	12	7	15	455	4	6	7	0	2	0	17	383	
452.55	30.83	1.92	0.12	0.63	0.21	0.00	1.14	1.11	0.47	18	21	142	3	40	8	767	0	7	3	12	147	3	7	17	0	0	0	5	279	
452.57	32.92	1.82	0.11	0.48	0.20	0.00	1.27	1.16	0.31	11	20	159	2	9	30	976	0	9	0	9	363	1	6	0	0	0	0	5	196	
452.74	32.69	4.17	0.23	0.51	0.16	0.00	2.09	0.79	0.14	15	22	182	1	65	27	1263	0	7	0	12	120	5	8	0	0	3	0	5	279	
452.76	33.28	1.76	0.17	0.41	0.15	0.00	1.20	0.63	0.13	13	19	122	4	35	19	566	19	9	0	7	152	2	4	9	0	2	0	3	157	
452.93	31.80	1.35	0.13	0.28	0.12	0.00	1.32	0.68	0.26	10	17	482	0	0	41	1289	10	12	0	9	201	2	7	10	0	2	2	5	189	
452.95	30.80	1.46	0.10	0.43	0.12	0.00	1.18	0.75	0.26	16	26	118	1	23	10	646	14	10	0	9	180	3	3	9	0	2	0	4	237	
453.12	26.12	1.03	0.07	0.41	0.13	0.00	0.69	0.47	0.08	16	21	39	0	73	13	205	0	10	0	8	296	4	3	0	0	2	0	4	168	
453.14	29.39	1.70	0.10	0.63	0.16	0.00	0.78	0.62	0.09	19	26	59	4	23	8	302	0	10	0	9	281	3	3	9	0	2	0	3	297	

The thin sections were stained with a combination of alizarin red and potassium ferricyanide to highlight carbonate mineralogy. Sodium cobalt-nitrite, barium chloride, and rhodizonic acid were applied to highlight plagioclase and potassium feldspars. Two sets of five thin sections were prepared. One set was covered by glass for petrographic analysis, and another set remained uncovered for microprobe analysis. The petrographic sections were examined under the 4× and 10× magnification lenses of the Nikon

Eclipse 50i POL microscope under polarized light and photographed using a Motic camera. The thin sections were prepared by AGAT Laboratories but analyzed at the University of Calgary.

Table 3
Samples location and approximate core depth of special core analysis for Well A (1AA 09-02-081-09 W4M).

	Depth	Petrography	XRD	EMPA	X-Ray Mapping	ICPM-MS	LA-ICPM-MS
Sample 449.7	449.70					Y	
Sample 1	451.00	Y	Y	Y	Y		
Sample 2	451.65	Y	Y	Y	Y	Y	* Y
Sample 3	451.93	Y	Y	Y	Y	Y	
Sample 4	452.09	Y	Y	Y	Y		
Sample 5	452.36	Y	Y	Y			

* continuous sample from ~451.5 m to ~ 451.8 m.

The mineralogical composition was also analyzed by XRD (Rigaku Multiflex XRD Diffractometer) at 40 kV and 40 mA, using a Cu K-alpha X-ray source at the Geoscience Research Laboratory of the University of Calgary. The samples were homogenized and milled prior to the mounting and analysis.

Feldspar compositions were determined using a JEOL JXA-8200 EMPA housed at the University of Calgary. For feldspars, the quantitative measurements of compositions were made using wavelength-dispersive X-ray spectroscopy (WDS) for Si, Al, Fe, Ca, Na, K, and Ba with an accelerating potential of 15 kV, a beam current of 20 nA, and a beam diameter of 5 µm. The measurements were calibrated using the following standards: K, Si, and Al on orthoclase standard, Na on albite standard, Ca on anorthite standard, and Fe on hornblende standard. The analyses were done on smooth surfaces and away from alterations and fractures. Raw counts were converted to concentrations using a ZAF correction protocol. Energy-dispersive X-ray spectrometry (EDS) was used for qualitative mineral identification. The WDS X-ray maps of U, Th, and Zr were used to locate the point sources of these elements in the sample.

Whole-rock geochemical analyses were accomplished on five samples at Bureau Veritas Commodities in Vancouver, British Columbia, Canada. Major elements were measured using inductively coupled atomic emission spectrometry (ICP-AES) and trace elements using ICP-MS, following lithium tetraborate fusion of the sample powders.

U–Pb dating of approximately 300 detrital zircon grains recovered from a 30-cm core section (from ~451.5 m to ~451.8 m; Fig. 5) from well A was done using laser ablation-inductively coupled plasma-mass spectrometry (LA-ICP-MS) at the University of Calgary. The sample material was treated with 30%–50% hydrogen peroxide to remove organic material prior to mineral separation. A full description of the measurement procedure, data reduction, and approach to filter the data is provided in Matthews and Guest (2017). Isotope signal intensities were measured using an Agilent 7700 quadrupole (ICP-MS) connected to a Resonetics RESOchron 193 nm excimer laser ablation system. Ablation occurred within a Laurin Technic M-50 dual volume ablation cell. All laser settings, dwell times for individual masses, gas flow rates, and ICP-MS settings can be found in the Supporting Information. For further information on the laser ablation system, the reader is referred to Müller et al. (2009). The well-characterized zircon reference material FC1 (Paces and Miller Jr, 1993) was used as the calibration reference material. Eight ablations for each of the three reference materials dated between 28.2 Ma and 1062.4 Ma were performed in each session to validate the results and assess uncertainties. Data reduction was handled in the commercially available Iolite software package (v2.5) (Paton et al., 2010) and a custom Excel VBA macro (ARS4.0). Uncertainty propagation was aligned with Horstwood et al. (2016), and all sources of uncertainty, both random and systematic, were propagated according to their best practices. The dates used for plotting and in the Discussion section are $^{206}\text{Pb}/^{238}\text{U}$ for dates less than 1200 Ma. The data were filtered for outliers using the probability of concordance calculated by the Concordia Age function in Isoplot (Ludwig, 1998, 2012). Measurements with less than 1% probability of concordance were eliminated from the data set. The measurements of 300 grains yielded 241 grains that passed the 1% probability of the concordance filter.

3.2. Analyses conducted on Wells 1, 2, and 3

A "hot" GR interval in well 1 was identified by a significant total GR spike reaching 270 API units (Fig. 3A), while in wells 2 and 3, it was recognized by a significant separation of shale volume curves

calculated from GR and neutron-density (Figs. 4 and 6). Facies analysis was conducted on slabbled cores using the same approach as for well A. Sampling was permitted only for the ICP-MS analysis of two samples in well 1 (Fig. 3A) and three samples in well 3 (Fig. 6). Additionally, high-resolution XRF data for well 2 (Fig. 4A) and well 3 (Fig. 6A) and a thin section from well 3 (Figs. 6C–F) were obtained from a publicly available database (AER Digital and Sample Repository Database), analyzed, and interpreted.

4. Results and interpretations

4.1. Lithology and ichnology of Well A

The sedimentary rocks of well A are represented by brown or black, oil-stained sandstone and light-gray mudstone. The bottom of the studied interval consists of approximately 0.5 m-thick cross-bedded sandstone (Fig. 5). The cross-bedded bottomsets exhibit flat-lying, non-bioturbated, light-gray mudstone at ~454.5 m that grades upward into darker colored, gently dipping (on Fig. 5: to the right), carbonaceous mudstone at ~454.4 m and thick, up to 30°-dipping, clean sandstone foresets towards the top of box 1. Core box 2 contains dm-scale cross-bedded sandstone with rip-up clasts at the base at ~453.71 m and/or fine-grained sandstone bottomsets at 453.4 m. The sedimentary rocks of box 3 are characterized by the interbedding of cross-bedded sandstone with fine-grained bottomsets (e.g., at 452.85, 452.75, and 452.55 m), ripple-laminated sandstone, and bioturbated mudstone at ~453.0 m. The sedimentary rocks of box 4 comprise fine-grained ripple cross-laminated sandstone grading into intensely bioturbated mudstone (BI = 6). Part of box 5 is missing, while the preserved 6 part consists of mixed, intensely bioturbated sandstone and mudstone. Box 6 contains almost exclusively ripple cross-laminated sandstone grading into bioturbated mudstone interbedded with thin sandstone and/or laminae, which continue into boxes 7 and 8 to approximately 448.15 m. Above 448.15 m, there is black, medium-grained, ripple cross-laminated sandstone. An overall fining-upward trend, coupled with an upwards decrease in the thickness of cross-beds and an increase in the presence of ripple cross-lamination, mud content, and bioturbation, is diagnostic of tidally influenced point-bar deposits of the McMurray Formation (Smith, 1989; Hubbard et al., 2011). In boxes 4–8, interbedded sandstone and mudstone are characteristic of IHS deposits formed in response to seasonal and/or decadal changes in flow and sediment influx (Smith, 1989; Jablonski and Dalrymple, 2016; Fustic et al., 2018). The brown-colored sandstone reflects a water-saturated zone with residual oil-stains, where a gas cap was present in the past, which was likely derived from the secondary microbial gas generation following petroleum entrapment (Fustic et al., 2013a; Fustic et al., 2019). Above it, black-colored sandstone (Box 8) is bitumen-saturated (Fustic et al., 2013a, Fustic et al., 2019).

Biodeformation structures may occupy 1/3–2/3 within a burrowed interval, and they are produced by near-surface grazing by small endobenthic organisms (e.g., Wetzel, 2009). Among the trace fossils, *Cylindrichnus*, *Planolites*, and *Skolithos* are rather common and characterized by the following details:

- *Cylindrichnus* is a slightly curved, downward tapering, vertical to inclined burrow with a mud-laminated wall and sand-filled causative tube. *Cylindrichnus* is characterized by a diameter of 0.4–0.8 cm and a length of 3–5 cm.
- *Planolites* is an unlined to rarely lined, straight to tortuous, circular to elliptical burrow with a variable diameter of 0.2–0.9 cm; its fill is structureless and differs from the host rock.
- *Skolithos* is a straight, simple, unbranched, vertical to sub-vertical tube with a uniform diameter of 4–6 mm.

Stratified sandstone and bioturbated mudstone have been interpreted to form within a fluvio-tidal system, precisely, in the inner to middle estuary or deltaic distributary channel. The deposition of sand occurred during high freshwater discharge episodes, facilitating dune migration, while mud accumulated during the periods of low discharge from tidally influenced, suspension-rich brackish water (Melynk and Gingras, 2020). Mud flocculation and deposition were fostered along the seawater-freshwater interface (e.g., La Croix and Dashtgard, 2014). Abundant bioturbation structures originating from the soles of the mudstone beds indicate marine influence in the estuary (e.g., Wetzel et al., 2017). Nonetheless, the burrows are rather small, and trace fossil diversity is low, implying stressed depositional setting (e.g., Pemberton et al., 1982; Wightman and Pemberton, 1997; Beynon and Pemberton, 1992; Buatois and Mángano, 2011).

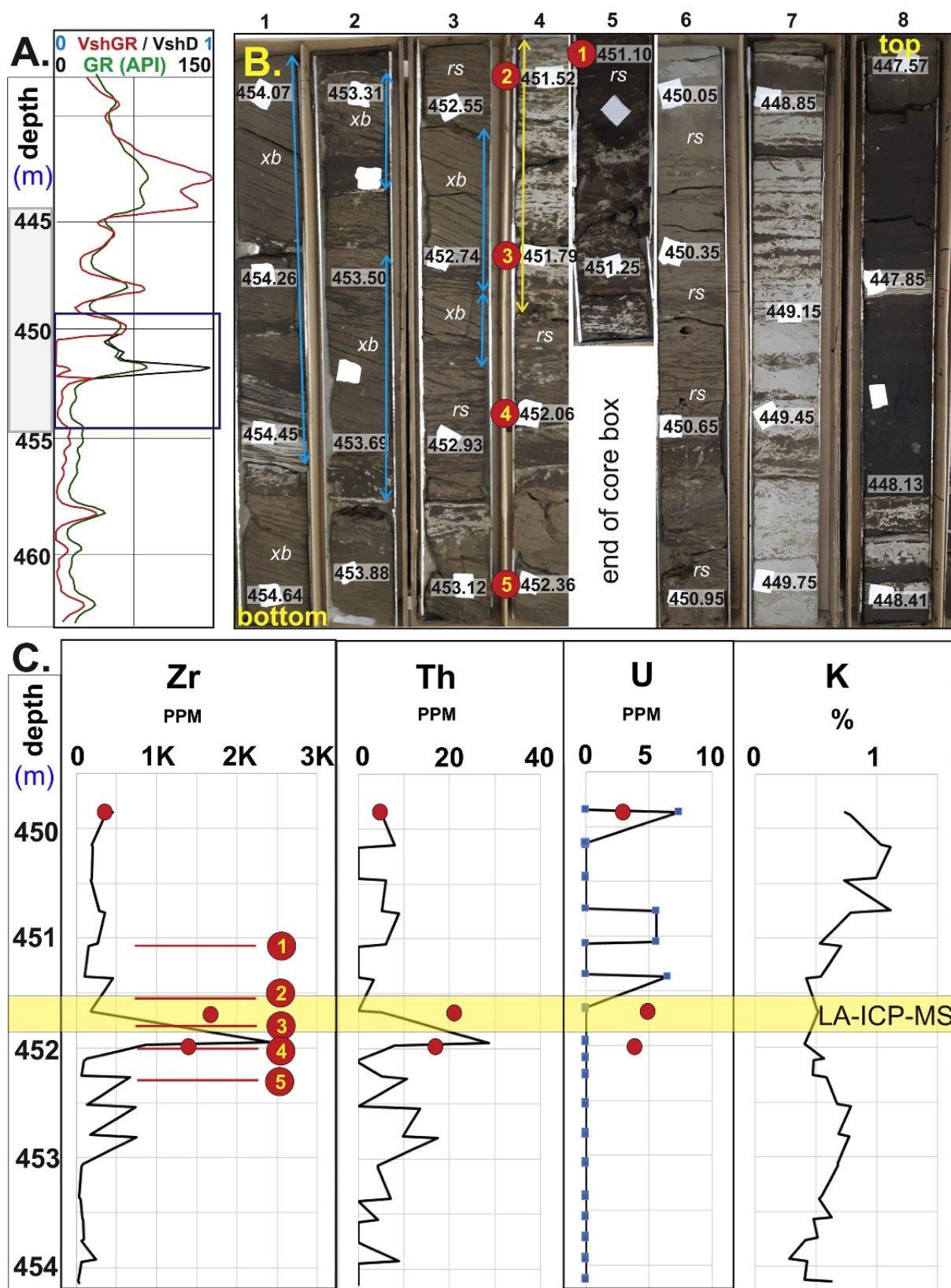


Fig. 5. Well A (1AA 09-02-081-09 W4M). A) GR and corresponding shale volume (Vsh) curves calculated from GR and density curves. Note a significant separation between VshGR (red) and VshDEN (black) between 450 and 452 m. characterized by values close to 0 and close to 1, respectively. Blue rectangle represents the whole core interval depicted in B. B) Core images from depths of 447.57–454.64 m with the interval of interest (~451.5–451.9 m). Key: black depth numbers—spots of spectral GR and XRF measurements; red circles—spots of special core analyses (XRD, petrography, and ICP-MS, see Table 4). The yellow arrow indicates an interval sampled for LA-ICP-MS. Blue arrows represent the thickness of individual cross-beds; rs – ripple cross-laminated sandstone; xb – cross-bedded sandstone. C) XRF concentrations of Zr (Zr, ppm), Th (Th, ppm), U (U, ppm), and K (K, %). Red dots show ICP-MS spots (Table 3). The yellow transparent box indicates an interval sampled for LA-ICP-MS.

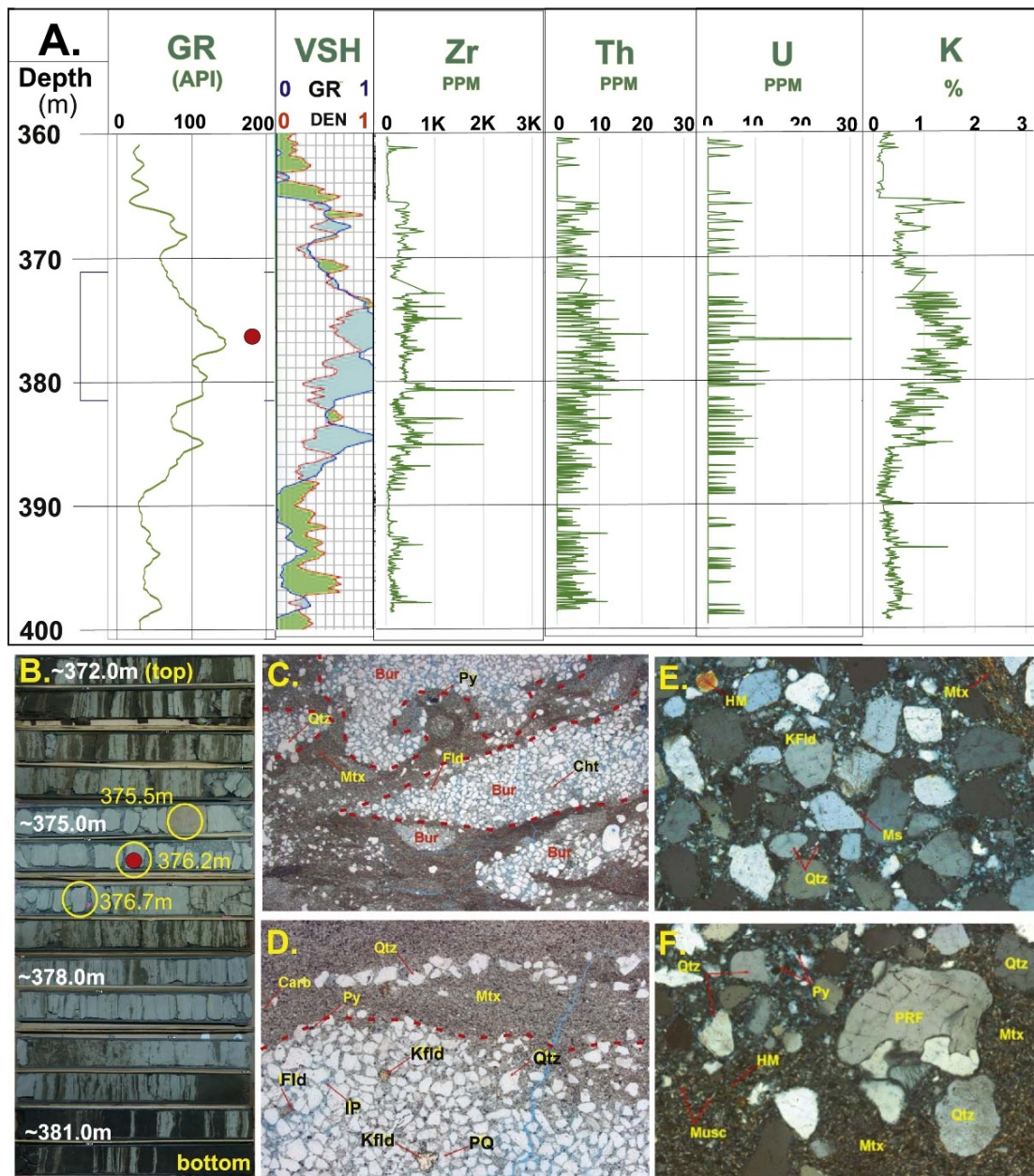


Fig. 6 Well 4 (1AA 14-14-076-07 W4M). A) GR log and geochemical data (360–400 m). Composite log: GR – gamma-ray, VSH – volume shale, DEN – density, ZR – zirconium, TH – thorium, U – uranium (in ppm from XRF), and K – potassium (in % from XRF). The blue rectangle shows the “hot” GR core interval depicted in (B); a red curved arrow shows vertical continuity of a single, large-scale point bar; a small red dot shows the location of the photomicrographs shown in (C–F). B) Core images of the “hot” GR interval (372.0–382 m) with the interval of interest (~375.0–377 m). Yellow circles show the location of ICP-MS samples (Table 4). Middle circle with red dot in the centre (at 376.2 m indicates thin section location for (C–F)). C) x12.5 PPL. Overview image of moderately to poorly sorted, burrowed (Bur) sandy siltstone (sublitharenite). Subangular to subrounded grains range in size from fine silt to upper coarse-grained sand. Framework grains are comprised of abundant quartz (Qtz – monocrystalline and minor polycrystalline), minor potassium and plagioclase feldspars (Fld), and traces of lithic grains, including chert (Cht), plutonic rock fragments (PRF). Accessory grains include minor carbonaceous debris, mica, and heavy mineral grains (i.e., rutile, tourmaline, epidote, and heavy minerals (HM). Secondary pyrite (Py) is disseminated throughout the matrix. Discrete pyrite framboids line some pores of the sandy burrows. D) x25 PPL view of a quartz-filled burrow and surrounding matrix (Mtx). Detrital quartz (Qtz) is also visible in a thin discontinuous lamination above the burrow. Additional detrital constituents: polycrystalline quartz (PQ), plagioclase feldspar (Fld), and potassium feldspar (KFld). Carbonaceous debris (Carb) and pyrite (Py) are disseminated. E) x100 XPL. High-magnification microphotograph of a quartz-rich burrow-fill. Qtz – quartz, KFld – potassium feldspar, Ms – muscovite, HM – heavy minerals, and Mtx – matrix. F) x400 XPL. High-magnification microphotograph of a burrow-fill, HM – heavy mineral, Note: PPL stands for transmitted, plain-polarized light; XPL stands for cross-polarized light. (For interpretation of the references to colour in this figure legend, the reader is referred to the web version of this article.)

4.2. Mineralogy of Well A

Petrographic analysis (Fig. 7) revealed the predominance of quartz (>98%) and minor amounts of K-feldspar (1%–2%) in the samples. Zircons were absent in sample 5, occurred in traces in samples 1 and 4, and were relatively abundant in samples 2 and 3 (Fig. 7 [top row]). Mudstone matrix was present in the bioturbated, zircon-enriched samples 2 and 3 (Fig. 7 [top row]). XRD analysis confirmed the dominance of quartz with some kaolinitic clays. K-feldspar was not detected in the XRD patterns due to its low proportion (<2%). Kaolinite is a common weathering product of feldspar; thus, small amounts of kaolinite detected in the XRD analyses may indirectly indicate the presence of K-feldspar (i.e., degraded feldspar).

4.3. Elemental composition and radioactive sources in Well A

The handheld spectral GR data showed low U concentrations (average 1.7 ppm; Table 1). These values were below the detection limit (~5 ppm) for the instrument and used cautiously. Similarly, Th showed a negligible variation with 2 minor spikes at depths of 450.95 and 451.79 m, located within the zone of interest (Figs. 5A–B). K concentrations also barely varied (0.4%–0.7%; Table 1).

The XRF data (Table 2, Fig. 5C) showed that Zr and Th showed an order of magnitude (~10×) increase within the interval of interest (Table 2, Fig. 5C), while U was below or close to the instrument detection limit (<7 ppm). K concentrations were low (Table 2, Fig. 5C) with subtle variability, consistent with the spectral GR data (Table 1).

The ICP-MS results (Fig. 5C; Table 4) indicated elevated elemental concentrations (less than two times in U, about two times in Th, and three times in Zr), while K concentration variability was minimal (Fig. 5C; Table 4). Similar trends obtained for the ICP-MS and XRF data (Fig. 5C) imply the reliability of XRF measurements.

Table 4
ICP-MS results for wells A, 1 and 3.

Well name	Depth	Th ppm	U ppm	K %	Zr ppm
1AA 09-02-081-09 W4M	449.7	10.0	2.8	1.33	457.1
1AA 09-02-081-09 W4M	451.7	21.4	5.0	1.12	1635.2
1AA 09-02-081-09 W4M	452.0	18.9	4.3	0.93	1333.9
1AA 01-12-076-07 W4M	377.5	10.2	2.9	0.77	933.3
1AA 01-12-076-07 W4M	377.7	40.7	8.4	0.64	4668.1
1AA 14-14-076-07 W4M	375.5	6.4	2.6	1.07	278.8
1AA 14-14-076-07 W4M	376.2	12.8	4.8	1.98	404.8
1AA 14-14-076-07 W4M	376.7	12.4	4.4	2.00	435.7

The WDS X-ray mapping results of thin sections (Fig. 8) illustrated that Zr concentrations were associated with zircon grains in the sampled interval. Furthermore, U and Th enrichment was almost exclusively associated with monazite grains (Fig. 8). This suggests that the horizons with high GR readings may be the zones of heavy mineral enrichment.

4.4. Sediment provenance and geochronology of Well 1

Sediment provenance was interpreted using thin-section petrography, mineralogy, and U–Pb geochronology. The predominance of well-sorted, sub-rounded to rounded quartz grains (Figs. 7–8) in the sandstone packages of the five studied samples strongly indicates high textural and compositional maturity.

The composition of feldspars was also used to distinguish between the plutonic, volcanic, and metamorphic sources. Out of the 74 EMPA spot analyses of feldspars, 67 were considered reliable (analytical total > 99 wt% and stoichiometrically consistent) and used for the interpretation (Table 5). In all samples, the orthoclase component was high (90%–93%), the albite component was minor (6%–9%), and the anorthite component was rare (<0.5%) (Fig. 9). These compositions imply metamorphic and plutonic rocks as feldspar sources (Trevena and Nash, 1981, p. 137; Fig. 11). This is consistent with

an origin from plutonic igneous rocks within the Canadian Shield or metamorphic rocks from the Grenville/Appalachian domain.

Table 5
Average electron-microprobe analyses (wt%) of K-feldspar for five selected samples from well A (Table 3; Fig. 5).

Al	1.01	1.01	1.02	1.02	1.02
Fe ²⁺	0	0	0	0	0
Ba	0.01	0.01	0.01	0	0.01
Ca	0	0	0	0	0
Na	0.07	0.06	0.07	0.07	0.1
K	0.93	0.93	0.92	0.93	0.9
Total Cations	5.01	5	5.01	5.01	5.01
Albite component	6.63	6.18	7.25	7.24	9.53
Anorthite component	0.07	0.15	0.1	0.04	0.2
Orthoclase component	93.3	93.67	92.65	92.72	90.28

n Total number of analyses that was averaged.

The detrital zircon U–Pb age-dating results (Fig. 10) showed that the population of zircons ranged from the Archean to the Paleozoic. The Archean-aged zircons were relatively rare, with most grains ranging from 2600 to 2800 Ma, and a few zircons were determined to be over 3000 Ma. The Mesoproterozoic-aged grains constituted the bulk of the zircon population, with the prominent 1000–1200 and 1600–1900 Ma signatures. A significant contribution from the 300–600 Ma zircons revealed the Paleozoic component and Appalachian orogen (300–600 Ma). This agrees with the sediment sources from the eastern parts of North America, where these rocks are exposed. Provenance of older grains is difficult to determine and beyond the scope of this study, but generally points to sources from Canadian Shield. Generally, this signature is also in line with detrital zircon populations previously reported from the middle McMurray Formation (Benyon et al., 2014, 2016; Blum and Pecha, 2014; Fig. 1B). Importantly, there was no evidence of Mesozoic and younger zircons characteristic of the Cordilleran magmatic or volcanic sources. Scattered zircon grains were notably smaller (< 30 µm) than quartz and feldspar grains (~100–200 µm; Figs. 7–8).

4.5. Lithology, mineralogy, elemental composition, and radioactive sources in Wells 1, 2, and 3

The intensely bioturbated (BI = 6) interval in Well 1 is approximately 0.3 m thick (Fig. 3A). It is characterized by a sharp GR spike reaching 270 API (Fig. 3A) and is overlain by a thick structureless and non-bioturbated (BI = 0) mudstone interval typical for the McMurray Formation abandoned-channel fills (Muwais and Smith, 1990; Fustic et al., 2013b). The sharp contact suggests either rapid abandonment by chute avulsion (Fustic et al., 2018) or an erosive cutbank of a younger channel. Dipmeter data (not available for this well) would allow for a definite conclusion (*sensu* Muwais and Smith, 1990). The intensely bioturbated interval in Well 2 is characterized by a GR spike reaching 200 API (Fig. 4A) and Vsh separation (Fig. 4A). The bioturbated interval forms part of a 35-m-thick, fining-upward sequence. A 20-m-thick interval (355–375 m; Fig. 4A) with unidirectionally oriented shallow dips (<10°) is indicative of IHS of a typical, large-scale (>30-m-thick) McMurray point-bar deposit (Fustic, 2007; Fustic et al., 2012; Brekke et al., 2017). Vsh separation in Well 3 (Fig. 6A) coincides with the top of a fining-upward cycle (Fig. 6A) and is indicative of the upper point bar composed of structureless and non-bioturbated light-gray mudstone (Fig. 6B). However, thin-section petrography reveals that this interval is intensely bioturbated (Fig. 6C–F).

The ICP-MS data showed that the concentrations of U, Th, and Zr in the interval of interest in Well 1 were approximately three times, four times, and more than five times higher than in surrounding layers, respectively. The concentration of K in the interval of interest varied little (Table 4). Although the ICP-MS results of Zr in Well 3 did not show any significant spikes (up to 435 ppm), higher-resolution XRF data revealed several localized spikes, with concentrations exceeding 1000 ppm (Fig. 6). The photomicrographs of Well 3 (Fig. 6C–F) showed not only the bimodal distribution of grains, in places where the matrix is characterized by silt and burrow-fill dominated by coarse-grained quartz, but they also presented heavy minerals, including zircons, within the burrow fill (Fig. 6C–F). The observed heavy mineral grains were significantly smaller than the quartz grains (Fig. 6C–F) due to the effects of hydraulic equivalence and sorting. Zircon grains (density 4.7 g/cm³) are much heavier than quartz (density 2.65 g/cm³), and the density contrast is enhanced when buoyancy is taken into account.

Therefore, hydraulic sorting in fluvial channels becomes even more effective (e.g., Best and Brayshaw, 1985). The observed difference in grain size between quartz and zircon grains matches the results of previous experimental studies (e.g., Tourtelot, 1968) as well as the observations of fluvial sandstones; in the latter case, zircons were found to be about 2ϕ smaller than concomitantly transported sand grains (e.g., Augustsson et al., 2019).

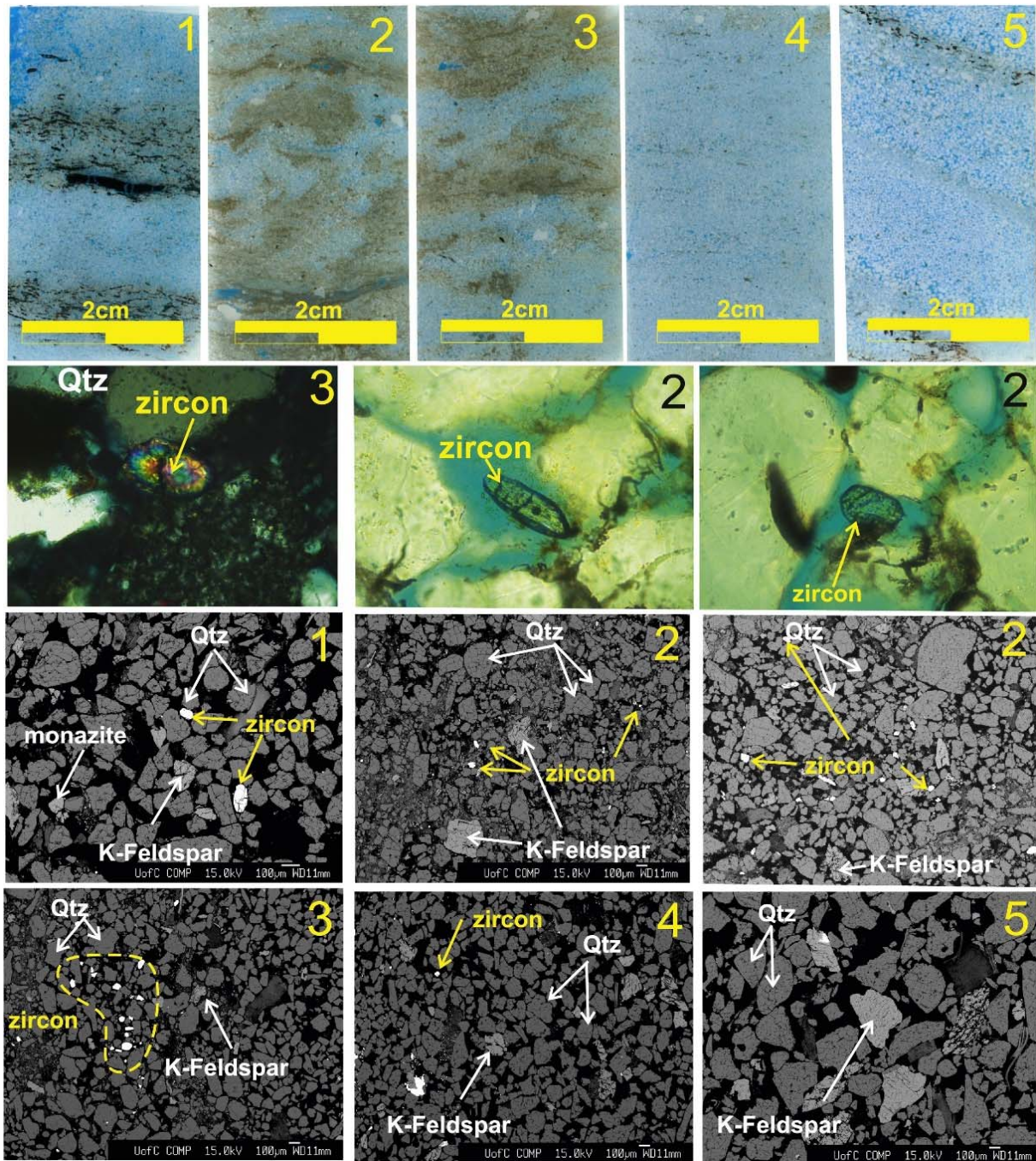


Fig. 7. Well A (1AA 09-02-081-09 W4M). Low-magnification images of selected thin sections (top row) and high-magnification photomicrographs of selected parts (zoomed in) in cross-polarized (top row) and plane-polarized lights (second row). The two bottom rows represent the backscattered electron images of the same thin sections. Numbers at the top right corner of each image indicate the sample number. Qtz-quartz, K-Fldp – potassium feldspar, yellow dashed line – a cluster of zircons. Sample depths can be found in Fig. 5. (For interpretation of the references to colour in this figure legend, the reader is referred to the web version of this article.)

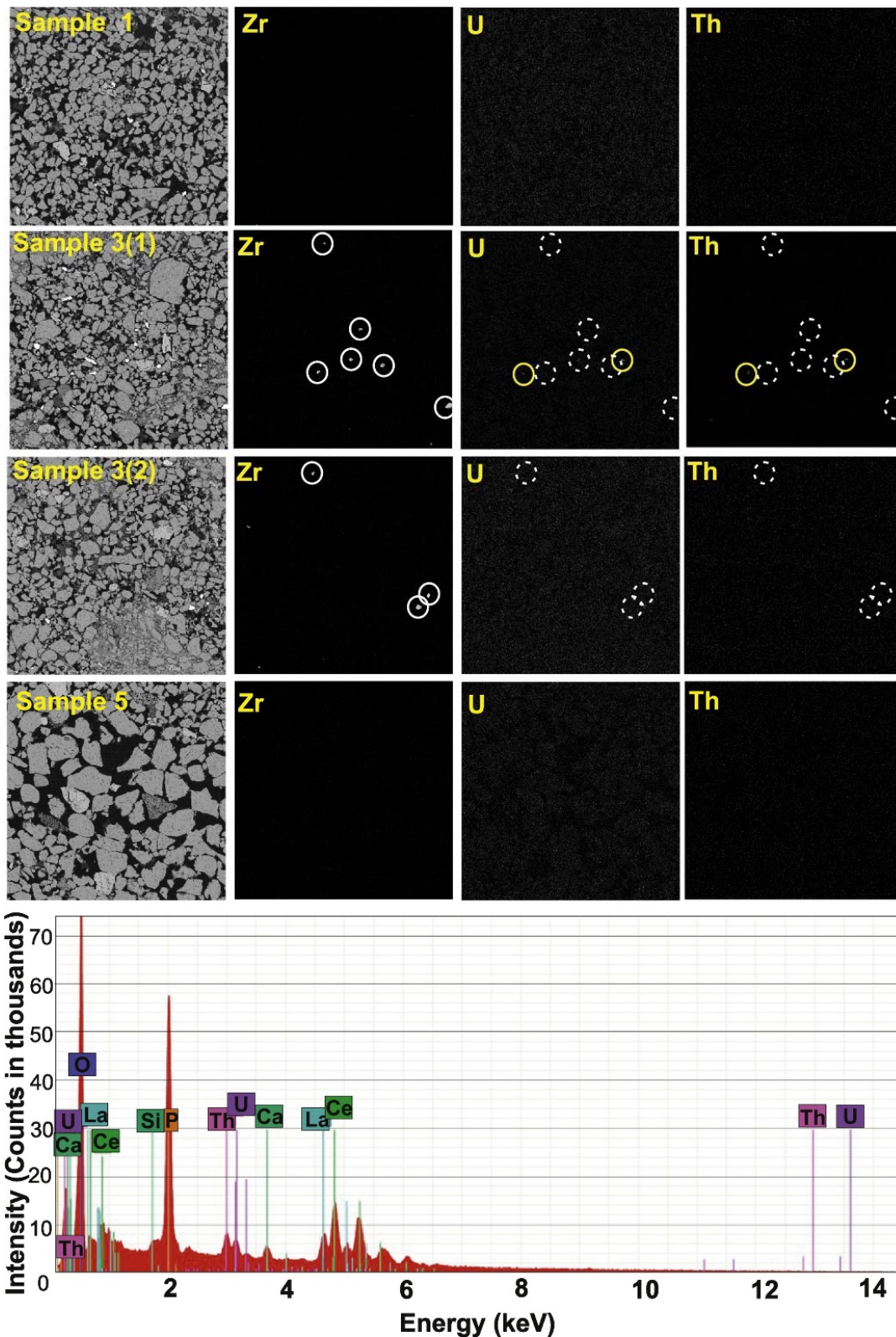


Fig. 8. Well A (1AA 09-02-081-09 W4M). Rows 1–4: Backscatter electron images and corresponding X-ray maps for Zr, U, and Th. The Zr, U, and Th signatures are associated with zircon grains and, in some cases, with monazite grains (U and Th). The sample depths are shown in Fig. 5. Sample 3 (rows 2 and 3) shows many bright spots (heavy minerals) in backscattered images. Some of them are zircon grains (white circles, Zr map), but none of the mapped zircon grains contains Th or U (see the positions of dashed white circles in U and Th maps). The two other grains (yellow and green circles) contain U and Th, but no Zr, suggesting they are monazite grains. Samples 1 and 5 are located above and below the interval of interest, respectively, and contain no heavy minerals. Row 5: Energy dispersive spectroscopy (EDS) of a monazite grain from Sample 3 (Fig. 5, Table 3). Note: U spikes are caused by monazite. (For interpretation of the references to colour in this figure legend, the reader is referred to the web version of this article.)

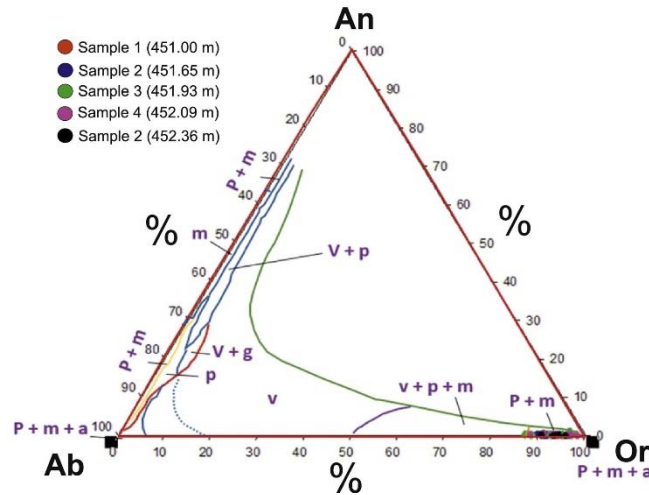


Fig. 9. Ternary diagram of Anortite, Albite, and Orthoclase (An-Ab-Or) showing the composition of K-feldspar from samples 1–5 (for sample locations refer to Fig. 5). The boundaries of volcanic; volcanic or plutonic; and volcanic, plutonic, or metamorphic provenance groups after Trevena and Nash, 1981, p. 142 and demonstrate a compositional range of eight provenance groups of feldspar. V – volcanic, p – plutonic, m – metamorphic, v + g – volcanic or granophyre, v + p – volcanic or plutonic, p + m – plutonic or metamorphic, v + p + m – volcanic, plutonic, or metamorphic, p + m + a – plutonic, metamorphic, or authigenic.

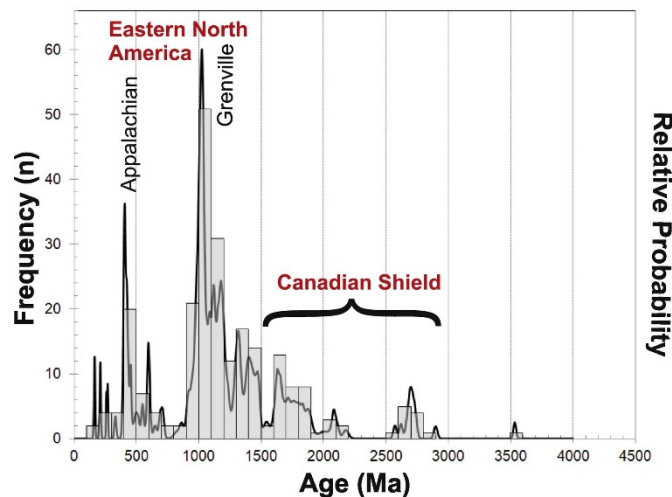


Fig. 10. Relative probability distribution of age ranges from 300 zircon measurements from a single sample, well A (sample location is shown in Fig. 5), showing the predominance of 300–600 Ma and ca. 1000–1200 Ma age of zircon grains. The grains were interpreted to be derived from the Appalachian and Grenville sources in eastern North America. A lesser amount of grains aged 1600–1900 Ma (Proterozoic) and ca. 2600–2800 Ma (Archean) were interpreted to be likely derived from the Canadian Shield. These results coincide with the basin-wide provenance studies of Benyon et al. (2014, 2016) and Blum and Pecha (2014).

4.6. Gamma-ray sources

The calibration of measurements obtained by wireline tools and analytical laboratory results, as well as the comparison between the two, were based on empirical observations. Standard industry conversion methods for calculating total GR (in API units) from U, Th, and K concentrations include equations developed by the American Petroleum Institute (API) and (Crain, 2006):

API equation:
$$\text{GR total} = 4 \times \text{THOR} + 8.1 \times \text{URAN} + 19.6 \times \text{POTA}, \quad (1)$$

Ross Crain equation:
$$\text{GR total} = 4 \times \text{THOR} + 8 \times \text{URAN} + 16 \times \text{POTA}, \quad (2)$$

where GR total is measured in the API units; URAN – uranium; THOR – thorium; and POTA – potassium. URAN and THOR are given in ppm and POTA in %.

Using the ICP-MS values obtained from Sample 3 at the depth of 451.93 in Well A (Table 4; Fig. 5C) in Eqs. (1) and (2), the yielded results are very similar to GR total measured in an open-hole (Fig. 5A):

$$\text{API equation:} \quad \text{GR total} = 4 \times 21.4 + 8.1 \times 5 + 19.6 \times 1.12 = 148.52 \quad (3)$$

$$\text{Ross Crain equation:} \quad \text{GR total} = 4 \times 21.4 + 8.0 \times 5 + 16.0 \times 1.12 = 145.50 \quad (4)$$

The same is true for the ICP-MS values obtained from Sample 2 at a depth of 377.7 m in Well 1 (Fig. 3), whereas Sample 1 in the same well (377.5 m) shows an anomalously low GR total value of approximately 75–80 API.

Sample 1:

$$377.5 \text{ m API equation:} \quad \text{GR total} = 4 \times 10.2 + 8.1 \times 2.9 + 19.6 \times 0.77 = 79.40 \quad (5)$$

$$377.7 \text{ m Ross Crain equation:} \quad \text{GR total} = 4 \times 10.2 + 8.0 \times 2.9 + 16.0 \times 0.77 = 76.30 \quad (6)$$

Sample 2:

$$377.5 \text{ m API equation:} \quad \text{GR total} = 4 \times 40.7 + 8.1 \times 8.4 + 19.6 \times 0.64 = 243.4 \quad (7)$$

$$377.7 \text{ m Ross Crain equation:} \quad \text{GR total} = 4 \times 40.7 + 8.0 \times 8.4 + 16.0 \times 0.64 = 240.2 \quad (8)$$

Distinguishing GR sources is an important screening method for revealing the presence of U and Th in heavy mineral grains, which are the subject of this study.

5. Discussion

Comparing continuous data, such as open-hole and sedimentary core logs, with results from micro- to nano-scale spot specific measurements or analyses taken at dm-scale distances from each other (e.g., spectral gamma, XRF, XRD, EMPA, EDS/X-Ray, ICP-MS) or homogenized samples (50-cm interval) may lead to apparent discrepancies. For example, continuous GR shale volume and density curve separation from ~450.5 to ~452 m (Fig. 5A) represents an intensely bioturbated interval (Fig. 5B), but spot-specific XRF and ICP-MS results show significant variations within this interval (Fig. 5C). Similarly, in Well 1 (Fig. 3A), the low content of U, Th, and Zr is observed adjacent to the samples with three-to-five times enrichment of these elements. It is suggested that radioactive zircon grains are concentrated within multiple thin (laminae-scale) bioturbated intervals and cause averaged, apparently continuous, open-hole log readings.

5.1. Sediment provenance

Mineralogical sample composition indicates that the sediments are mature and are dominated by quartz with minimal amounts of feldspars and clay minerals, suggesting prolonged transport. Detrital zircon age constraints (using geochronology) indicate that the sources were located in eastern North America, including the Canadian Shield, Appalachian, Grenville, and Trans-Hudson orogens (Fig. 10). This implies long (many tens to hundreds of kilometers) transport distances. The relatively low amounts of feldspar and the presence of kaolinitic clays may indicate prolonged exposure and weathering processes or, more likely, increased maturity due to multiple reworking cycles by rivers and tides in the McMurray Formation's low accommodation setting (Leckie et al., 2009). This scenario agrees with the fact that zircon is an ultrastable heavy mineral and can survive several cycles of exhumation, weathering, transport, and burial. Zircons are characterized by low fissility and very low solubility over a wide range of pH values. Consequently, if the catchment area is stable and subject to very slow denudation, the parent material resides for a considerable amount of time within the weathering zone, and very stable

heavy minerals (e.g., zircon, rutile, tourmaline) may become enriched. This scenario appears possible for the Canadian Shield (Fig. 1B) during the Mesozoic.

Previous regional provenance studies of the McMurray Formation were based on zircons obtained from clean, cross-bedded sandstone deposited in high-energy settings, such as a channel base (Benyon et al., 2014, 2016; Blum and Pecha, 2014; Fig. 1B). The utilized sampling strategy assumed that most zircons and other heavy minerals were hydrodynamically concentrated in high-energy settings. However, the XRF results presented herein (Figs. 4–6) show that the strongest Zr signal is commonly associated with fine-grained, intensely bioturbated sediments of the upper point bar (Figs. 3–6), implying that fine-grained strata are also good targets for detrital zircon geochronologic studies.

5.2. Radioactive sources

The reproduction of the GR total values (see Section 4.6) shows that heavy minerals sourced Th and U radiation are major contributor of natural radioactivity in the “hot” GR zones. More ICP-MS data points would provide a more valid statistical model.

The assumption that most, if not all, Zr spikes in the IHS intervals recorded by XRF (Figs. 4–6) are caused by zircon grains and, consequently, most, if not all, Th and U spikes are caused by emissions from zircon grains, leads to several questions: (i) What does the fining-upward log pattern really represent?, and (ii) Since the content of measured K in most cases (Fig. 5) is low and likely not sufficient to recalculate the recorded total GR, does it really represent the increased clay content, as commonly suggested, or is it a function of zircon grains dispersed in fine-grained sediments? Answers to these questions are beyond the scope of this work and need to be addressed in the future.

A comparison of the API values of GR spikes with the corresponding shale baselines (Fig. 3) and Vsh density curve suggests that, in anomalous areas, U and Th contribute to an increase in GR readings up to three times of baseline value. The removal of U from API calculations for Samples 1–3 (Section 4.6) shows a decrease of approximately 30% of the total calculated API units.

$$\text{Sample 1 (U+Th+K) GR total} = 4 \times 10.2 + 8.1 \times 2.9 + 19.6 \times 0.77 = 79.40 \text{ (9)}$$

$$\text{Sample 1 (Th+K) GR total} = 4 \times 10.2 + 8.1 \times 0.0 + 19.6 \times 0.77 = 55.90 \text{ (30\%decrease) (10)}$$

$$\text{Sample 2 (U+Th+K) GR total} = 4 \times 40.7 + 8.1 \times 8.4 + 19.6 \times 0.64 = 243.4 \text{ (11)}$$

$$\text{Sample 2 (Th+K) GR total} = 4 \times 40.7 + 8.1 \times 0.0 + 19.6 \times 0.64 = 175.55 \text{ (28\%decrease) (12)}$$

$$\text{Sample 3 (U+Th+K) GR total} = 4 \times 21.4 + 8.1 \times 5.0 + 19.6 \times 1.12 = 148.52 \text{ (13)}$$

$$\text{Sample 3 (Th+K) GR total} = 4 \times 21.4 + 8.1 \times 0.0 + 19.6 \times 1.12 = 107.55 \text{ (28\%decrease) (14)}$$

5.3. Possible mechanisms of zircon concentrations

Zr is transported by rivers in dissolved, colloidal, and particulate forms. It preferably precipitates and concentrates in brackish waters (Schneider et al., 2016), analogous to the tidally influenced McMurray Formation deposits. The interdependence of Zr and the biosphere is not well understood. Essentially, Zr behaves like a trace element in the biosphere, where it occurs in higher amounts than most other trace elements (Ghosh et al., 1992). Zr is taken up by plants from soil and water, and it accumulates in certain tissues (Ghosh et al., 1992). Its abundance in Bulgarian coals is explained by the enrichment in tissues of precursors (Eskenazy, 1987). The relationship of zircon grains and biosphere is poorly documented, except for the evidence of selective zircon accumulations in *Psammophaga zirconia* – benthic foraminifera living in the modern Adriatic and Black Seas (Sabbatini et al., 2016). In many instances, ashfalls provide enormous amounts of mineral nutrients, which strongly impact the biosphere, initiating algal blooms and consuming oxygen in the water column. The processes mentioned above cause ideal conditions for the preservation of organic matter (Lee et al., 2018). Ashfalls can also enhance environmental conditions and indirectly impact benthic fauna (e.g., Wetzel, 2008, 2009).

Elemental mapping of the samples (Fig. 8) illustrates that Zr is associated with zircon grains (Fig. 8). However, this does not rule out the possibility that some Zr was concentrated by other above-mentioned processes elsewhere in the McMurray Formation. The results of this study suggest that anomalous GR log signatures can be associated with strongly bioturbated mudstone and/or fine-grained sandstone with unusual concentrations of heavy minerals, in particular, of zircon and monazite (Figs. 6–8). Zircon enrichment in sediments may involve a combination of source characteristics, weathering, and/or hydraulic sorting. The lack of syndepositional ages in the detrital zircon population does not support enrichment by a Zr-rich syndepositional source, such as volcanic ash.

The concentration of zircon and monazite by hydraulic sorting can occur due to the high density of these minerals. The grain-size and abundance analyses of heavy minerals suggest that in some settings, such as alluvial fans, zircon grains may preferentially concentrate in the fine-grained heavy mineral fraction (Potter, 1955; Hou et al., 2011). Similarly, turbidite sandstone beds can show normal or inverse grading if the heavy minerals are abundant. The type of grading depends on the density of the heavy minerals (von Rad, 1972). Zircon tends to be enriched in the fine-grained sandstone fraction, while the concentration of other heavy minerals decreases concomitantly upward (von Rad, 1972).

The ancient McMurray River system represented a typical continental-scale river that flowed over a very long distance (Fig. 1B). Most of its course likely had a low gradient, and sediment sorting was efficient (e.g., Miall, 1996). Thus, fine-grained IHS of upper point bars (Fig. 11A–B) may have been subjected to heavy mineral enrichment by hydraulic processes and associated grain sorting based on the hydraulic equivalence (e.g., Miller and Miller, 2007). However, hydraulics alone cannot explain why the highest concentrations occur in the most bioturbated intervals (Figs. 3–6). This aspect is addressed below.

The significantly elevated natural radioactivity is related to an increased zircon content in the examined intensely bioturbated fine-grained strata (Figs. 3–6), wherein the zircon grains are randomly distributed (Figs. 7–8) rather than stratified as a result of hydrodynamic sorting. Neochronological studies have shown that burrowing organisms do not only disturb primary sedimentary structures but may also cause sediment re-suspension and modify a relatively smooth sediment-water interface into an irregular surface, exhibiting enhanced roughness due to the newly formed cones and funnels (e.g., Sanford, 2008; Han et al., 2019). Furthermore, if exposed on the surface at low to moderate densities (e.g., Eckman et al., 1981), the lined tubes may affect the flow and enhance sediment reworking (e.g., Carey, 1983; Nowell and Jumars, 1984). As a consequence, the current flow along the sediment-water interface becomes more turbulent and unsteady. As such, fine particles can entrain into suspension and be transported by traction and/or saltation (e.g., Nowell and Jumars, 1984; Vogel, 1994). Bioturbation is known to significantly modulate the IHS of the upper point-bar deposits in the Middle McMurray Formation (Figs. 11A–B). Following the deposition on the lateral or downstream accretion surface (Fig. 11B), burrowing organisms disturb sediments, re-suspend clay and silt particles, and generate a rough surface, which in turn helps create a turbulent flow (Fig. 13C). Furthermore, biogenic sediment mixing causes repeated turnover of the inhabited sediment layer (“mixed layer”). Hence, the particles exposed on the surface are subjected to multiple hydraulic sorting cycles (e.g., Gérino et al., 2003). The increased turbulence leads to even more particles become suspended and initiates bedload transport of heavier grains, including zircons, by traction and saltation (Fig. 11C). The heavy grains then become rapidly trapped by the gravity force in numerous burrows (Fig. 11C). Due to the permanent sediment reworking and removal of fine particles, the beds aggrade slowly, and the proportion of heavy grains, including zircon, increases (Fig. 11D). These processes occur simultaneously and recurrently (Fig. 11E), in particular, during the freshet and waning-flood stages.

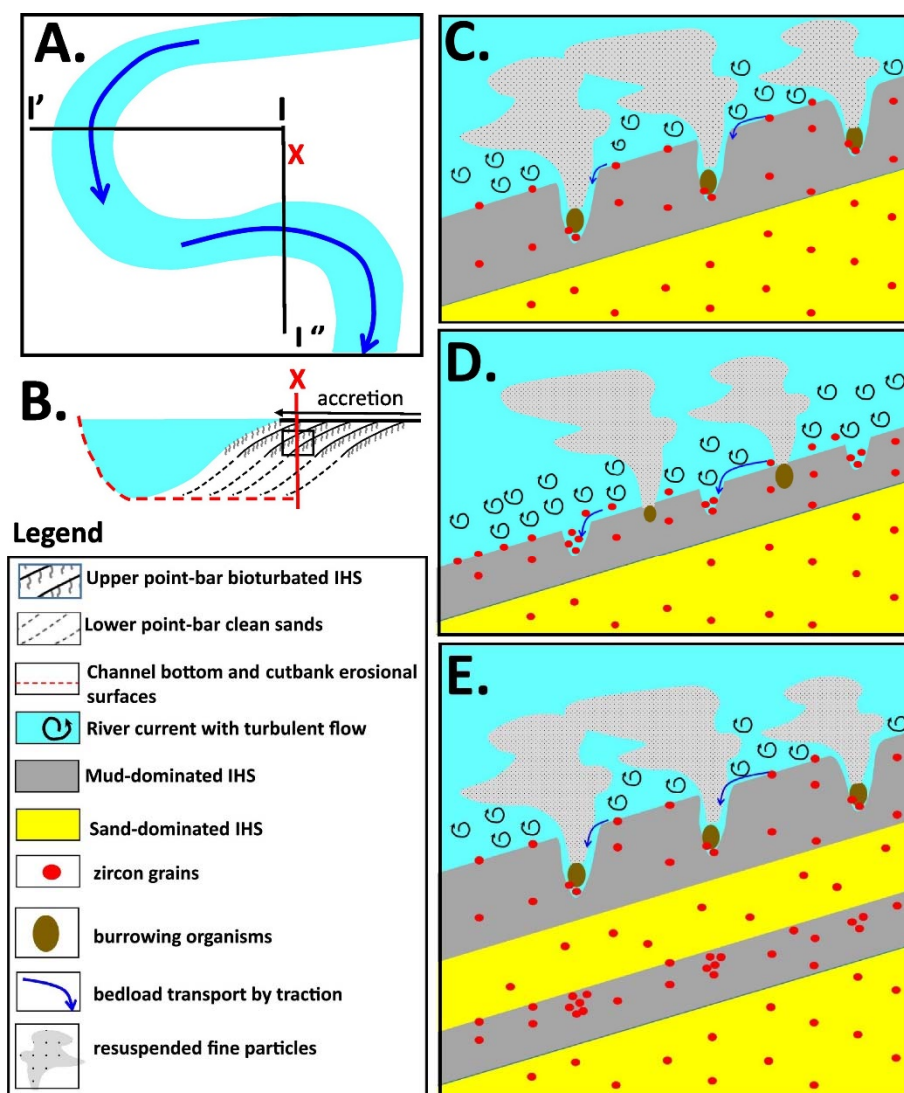


Fig. 11. A schematic (not to scale) and simplified diagram representing the interpreted geological setting (A–B) and key geological events causing zircon concentration in fine-grained IHS of the upper point-bar deposits of the Middle McMurray Formation (C–D). Key: X—a hypothetical location of wells shown in Figs. 1 and 4–5. A) Sketch of a typical (up to 5-km-wide) McMurray Formation point bar characterized by both lateral and downstream accretion (Smith et al., 2009; Hubbard et al., 2011; Fustic et al., 2012). B) Cross-section through lateral (I-I') or downstream (I-I'') accretion sets of a point bar in (A). The black rectangle shows the point-bar location illustrated in (C–E). Note that typical IHS dips range between 3° and 11°. C) Processes occurring along the sediment-water interface with the input from vertical burrows (e.g., *Skolithos*, *Cylindrichnus*), re-suspension of fine particles, the occurrence of turbulent flows due to increased surface roughness, bedload transport, zircon trapping in burrows, and inferred downstream removal of fine-grained particles. Note: in a dynamic setting, all processes occur simultaneously. D) Processes described in (C) result in progressive “thinning” of original strata and enrichment of zircon grains. E) Following the next (likely seasonal) high-flow conditions and deposition of sand, the mudstone enriched with zircons is buried, and a new mud-dominated unit gets deposited. The processes described in (C–D) re-occur.

X-ray microtomography (Micro-CT; Baniak et al., 2014) would help visualize in 3-D the proposed zircon trapping in burrows. More high-resolution sampling would allow for better statistical data representation. A comparison of zircon concentrations in the lower versus upper point-bar deposits might shed new light on the hydrodynamic sorting of grains in high-energy versus low-energy depositional settings. Similar studies in other sedimentary basins, stratigraphic units, and laboratory experiments involving flume tanks and microcosm sediments with heavy minerals and introduced burrowing organisms (*sensu* Herringshaw and McIlroy, 2013) are expected to demonstrate that the proposed mechanism is universal. Literature review lacks studies describing the potential impact of volcanic ashfalls on the intensity of bioturbation in brackish-water settings. Although nutrient

availability in brackish-water settings usually is not a limiting factor, such study may provide new insights about the interdependence of physical processes and the biosphere.

6. Conclusions

Contrary to the conventional wisdom that increased radioactivity (i.e., "hot" GR) in fine-grained strata is almost exclusively caused by an increased potassium content present in clay minerals, our study shows that GR spikes can be caused by increased concentration of zircon and/ or monazite grains. Zircon and monazite grains are commonly entrained in heavy mineral fractions during fluvial transport and may get entrapped in sandy fractions under favorable conditions.

The zircon age distribution is consistent with other samples from the Middle McMurray channel deposits, suggesting the Canadian Shield, Appalachian, and Grenville sources. The analyzed samples provide no evidence for syndepositional zircons from late-stage Cordilleran volcanism or local kimberlite eruptions. The association of zirconium in the samples to zircon grains rules out significant zirconium transport by river systems in dissolved, colloidal, and particulate forms and later precipitation in fine-grained upper point-bar deposits. Instead, based on the integration of the geochemical and petrographic data, sedimentary facies analysis, and detrital zircon geochronology, we envisage an interplay of hydraulic sorting and bioturbation leading to the entrapment of zircons and other heavy minerals in the studied "hot" GR intervals. The distinct association of the "hot" GR intervals with high intensity of bioturbation suggests that zircon grains within the IHS of the upper point-bar deposits may get entrapped in burrows through the preferential removal of lighter grains by re-suspension due to burrowing.

The proposed explanation may apply to the other intervals characterized by similar GR and/or Zr spikes across the McMurray Formation. To the best knowledge of authors, this is the first documentation of zircon-grain entrapment caused by bioturbation. These findings may be applicable to other heavy mineral fractions in similar depositional settings. Implications to reservoir characterization studies might also be significant.

Declaration of Competing Interest The authors whose names are listed immediately below certify that they have NO affiliations with or involvement in any organization or entity with any financial interest (such as honoraria; educational grants; participation in speakers' bureaus; membership, employment, consultancies, stock ownership, or other equity interest; and expert testimony or patent-licensing arrangements), or non-financial interest (such as personal or professional relationships, affiliations, knowledge or beliefs) in the subject matter or materials discussed in this manuscript.

Acknowledgments

We sincerely thank many colleagues and friends who have helped during analytical work and/or have provided useful directions and feedback over the last two years. We particularly thank Dr. Rudi Meyer and Rob Marr (University of Calgary), Dr. Dennis Meloche (Independent), Tim Hartel (RockProof), Tom Weedmark and Dr. Ron Spencer (XRF Solutions), Omid Hardakani, Pavel Kabanov and Richard Vandenberg (Geological Survey of Canada), Bryce Jablonski (CNRL), Astrid Arts (Cenovus Energy), Sergei Vasinda (GranTierra), Jim Koch (Independent), Shengyu Li (Chengdu University), and Graham Spray (AGAT Laboratories). AER Core Storage is thanked for a significant academic discount for viewing, examining, and sampling selected cores, GeoLOGIC Systems for access to petrophysical logs, AGAT Laboratories for preparing thin sections, University of Calgary Laboratories for access to EMPA, EDS, LA-ICP-MS and petrographic microscopy labs, and Bureau Veritas Commodities Canada Ltd. for ICP-MS analysis. Dr. Andrew Leier and Dr. Alina Shchepetkina as well as Dr. Thomas Algeo (Editor-in-Chief) are sincerely thanked for thorough reviews and constructive suggestions that have significantly improved the final version of the manuscript.

References

- Alberta Energy Regulator, 2015. Alberta's energy reserves 2014 and supply/demand outlook 2015–2024. In: Statistical Series (ST) 2015–98.
- Augustsson, C., Aehnelt, M., Voigt, T., Kunkel, C., Meyer, M., Schellhorn, F., 2019. Quartz and zircon decoupling in sandstone: petrography and quartz cathodoluminescence of the Early Triassic continental Buntsandstein Group in Germany. *Sedimentology* 66 (7), 2874–2893.
- Baniak, G.M., Gingras, M.K., Burns, B.A., George Pemberton, S., 2014. An example of a highly bioturbated, storm-influenced shoreface deposit: upper Jurassic Ula Formation, Norwegian North Sea. *Sedimentology* 61 (5), 1261–1285.
- Benyon, C., Leier, A., Leckie, D.A., Webb, A., Hubbard, S.M., Gehrels, G., 2014. Provenance of the Cretaceous Athabasca Oil Sands, Canada: implications for continental-scale sediment transport. *J. Sediment. Res.* 84 (2), 136–143.
- Benyon, C., Leier, A.L., Leckie, D.A., Hubbard, S.M., Gehrels, G.E., 2016. Sandstone provenance and insights into the paleogeography of the McMurray Formation from detrital zircon geochronology, Athabasca Oil Sands, Canada. *AAPG Bull.* 100 (2), 269–287.
- Best, J.L., Brayshaw, A.C., 1985. Flow separation – a physical process for the concentration of heavy minerals within alluvial channels. *J. Geol. Soc. Lond.* 142 (5), 747–755.
- Beynon, B.M., Pemberton, S.G., 1992. Ichnological signature of a brackish water deposit: an example from the Lower Cretaceous Grand Rapids Formation, Cold Lake oil sands area, Alberta. In: Pemberton, S.G. (Ed.), *Applications of Ichnology to Petroleum Exploration*. Society of Economic Geologists and Paleontologists, Core Workshop 17, pp. 199–221.
- Blum, M., Pecha, M., 2014. Mid-Cretaceous to Paleocene North American drainage reorganization from detrital zircons. *Geology* 42 (7), 607–610.
- Brekke, H., Evoy, R.W., 2004. Implications of dipmeter data for the definition of the internal architecture in point-bar deposits from the Athabasca oil sands. In: *Canadian Society of Petroleum Geologists (CSPG) Annual Meeting, Calgary, Alberta, Program and Abstracts CD*.
- Brekke, H., MacEachern, J.A., Roenitz, T., Dashtgard, S.E., 2017. The use of microresistivity image logs for facies interpretations: an example in point-bar deposits of the McMurray Formation, Alberta, Canada. *AAPG Bull.* 101 (5), 655–682.
- Broughton, P.L., 2016. Collapse-induced fluidization structures in the Lower Cretaceous Athabasca Oil Sands Deposit, Western Canada. *Basin Res.* 28 (4), 507–535.
- Broughton, P.L., 2018. Salt tectonism and distribution of brackish-water trace fossils in the Cretaceous McMurray Formation, Athabasca Oil Sands, Alberta Foreland Basin. *Can. J. Earth Sci.* 55 (12), 1354–1383.
- Buatois, L.A., Mángano, M.G., 2011. *Ichnology: Organism-Substrate Interactions in Space and Time*. Cambridge University Press.
- Carey, D.A., 1983. Particle resuspension in the benthic boundary layer induced by flow around polychaete tubes. *Can. J. Fish. Aquat. Sci.* 40 (S1), s301–s308.
- Carrigy, M., 1959. *Geology of the McMurray Formation; Part III. General Geology of the McMurray area (RPRT)*. Alberta Geological Survey Memoir. Alberta Geological Survey, Edmonton, Canada.
- Crain, E.R., 2006. Crain's Petrophysical Pocket Pal. ER Ross, Ontario. Dickinson, W.R., Gehrels, G.E., 2009. Use of U–Pb ages of detrital zircons to infer maximum depositional ages of strata: a test against a Colorado Plateau Mesozoic database. *Earth and Planetary Science Letters* 288 (1–2), 115–125.
- Eccles, D., 2011. *Northern Alberta Kimberlite Province: The First 20 Years: Energy Resources Conservation Board*.
- Eckman, J.E., Nowell, A.R., Jumars, P.A., 1981. Sediment destabilization by animal tubes. *J. Mar. Res.* 39 (2), 361–373.

- Eskenazy, G.M., 1987. Zirconium and hafnium in Bulgarian coals. *Fuel* 66 (12), 1652–1657.
- Flach, P.D., Wightman, D.M., Brown, R.K., Fustic, M., 2020. Observations on Transgression, Regression and Sequence Stratigraphy in the McMurray Formation. Athabasca Oil Sands Area.
- Fustic, M., 2007. Stratigraphic dip analysis—a novel application for detailed geological modeling of point bars, and predicting bitumen grade, McMurray Formation, Muskeg River Mine, northeast Alberta. *Nat. Resour. Res.* 16 (1), 31–43.
- Fustic, M., Hubbard, S.M., Spencer, R., Smith, D.G., Leckie, D.A., Bennett, B., Larter, S., 2012. Recognition of down-valley translation in tidally influenced meandering fluvial deposits, Athabasca Oil Sands (Cretaceous), Alberta, Canada. *Mar. Pet. Geol.* 29 (1), 219–232.
- Fustic, M., Bennett, B., Huang, H., Oldenburg, T., Hubbard, S.R., Larter, S., 2013a. Impact of oil-water contacts, reservoir (dis)continuity, and reservoir characteristics on spatial distribution of water, gas, and high-water – low-bitumen saturated zones and variability of bitumen properties in Athabasca oil sands deposits. In: Hein, F.J., Leckie, D.A., Larter, S., Suter, J. (Eds.), *Heavy Oil/Bitumen Petroleum Systems in Alberta and beyond*, AAPG Studies in Geology 64, pp. 163–205.
- Fustic, M., Cadiou, D., Thurston, D., Al-Dliwe, A., Leckie, D.A., 2013b. Reservoir modeling by constraining stochastic simulation to deterministically interpreted three-dimensional geobodies: case study from Lower Cretaceous McMurray Formation, Long Lake steam-assisted gravity drainage project, Northeast Alberta, Canada. In: Hein, F.J., Leckie, D., Larter, S., Suter, J.R. (Eds.), *Heavy Oil and Oil Sand Petroleum Systems in Alberta and beyond*, AAPG Studies in Geology, 64, pp. 565–604.
- Fustic, M., Strobl, R., Ghinassi, M., Zhang, S., 2018. Unsuccessful cut offs – origin and partial preservation of enigmatic channels encased within a large-scale point bar deposit with implications to Reservoir Developments, the McMurray Formation type section, Alberta, Canada. In: Ghinassi, Massimiliano, Colombera, Luca, Mountney, Nigel, Reesink, Arnold Jan H. (Eds.), *Fluvial Meanders and Their Sedimentary Products in the Rock Record*. International Association of Sedimentologists, Special Publication 48. John Wiley & Sons Ltd., pp. 321–347
- Fustic, M., Strobl, R., Fowler, M., Jablonski, B.V., Martinius, A.W., 2019. Impact of reservoir heterogeneity on oil migration and the origin of oil-water contacts: McMurray Formation type section, Alberta, Canada. *Mar. Pet. Geol.* 103, 216–230.
- Gérino, M., Stora, G., Francois, F., Gilbert, F., Poggiale, J.-C., Mermillod-Blondin, F., Desrosiers, G., Vervier, P., 2003. Macro-invertebrate functional groups in freshwater and marine sediments: a common mechanistic classification. *Vie et milieu* 53 (4), 221–232.
- Ghinassi, M., Ielpi, A., Aldinucci, M., Fustic, M., 2016. Downstream-migrating fluvial point bars in the rock record. *Sediment. Geol.* 334, 66–96.
- Ghosh, S., Sharma, A., Talukder, G., 1992. Zirconium. *Biol. Trace Elem. Res.* 35 (3), 247–271.
- Gingras, M.K., Baniak, G., Gordon, J., Hovikoski, J., Konhauser, K.O., La Croix, A., Lemiski, R., Mendoza, C., Pemberton, S.G., Polo, C., Zonneveld, J.-P., 2012. Porosity and permeability in bioturbated sediments. In: Knaust, D., Bromley, R.G. (Eds.), *Trace Fossils as Indicators of Sedimentary Environments*. Developments in Sedimentology, vol. 64. Elsevier, pp. 837–868.
- Gingras, M.K., MacEachern, J.A., Dashtgard, S.E., Ranger, M.J., Pemberton, S.G., Hein, F., 2016. The significance of trace fossils in the McMurray Formation, Alberta, Canada. *Bull. Can. Petrol. Geol.* 64 (2), 233–250.
- Han, X., Fang, H., Johnson, M.F., Rice, S.P., 2019. The impact of biological bedforms on near-bed and subsurface flow: a laboratory-evaluated numerical study of flow in the vicinity of pits and mounds. *J. Geophys. Res.* 124 (7), 1939–1957.
- Hein, F.J., Berhane, H., Cotterill, D.K., 2000. An atlas of lithofacies of the McMurray Formation Athabasca oil sands deposit, northeastern Alberta: surface and subsurface. Energy and Utilities Board, Edmonton, AB: Alberta, p. 216.
- Hein, F.J., Cotterill, D.K., 2006. The Athabasca oil sands – a regional geological perspective, Fort McMurray area, Alberta, Canada. *Nat. Resour. Res.* 15 (2), 85–102.

- Hein, F.J., Dolby, G., Fairgrieve, B., 2013. A regional geologic framework for the Athabasca oil sands, northeastern Alberta, Canada. In: Hein, F.J., Leckie, D.A., Larter, S., Suter, J. (Eds.), *Heavy Oil/Bitumen Petroleum Systems in Alberta and beyond*, AAPG Studies in Geology 64, pp. 207–250.
- Hein, F.J., Langenberg, C.W., Kidston, C., Berhane, H., Berezniuk, T., Cotterill, D.K., 2001. A comprehensive field guide for facies characterization of the Athabasca oil sands, northeast Alberta. Alberta Energy and Utilities Board Special Report 13, 415.
- Herringshaw, L.G., McIlroy, D., 2013. Bioinfiltration: Irrigation-driven transport of clay particles through bioturbated sediments. *J. Sediment. Res.* 83 (6), 443–450.
- Horner, S.C., Hubbard, S.M., Martin, H.K., Hagstrom, C.A., 2019. Reconstructing basin-scale drainage dynamics with regional subsurface mapping and channel-bar scaling, Aptian, Western Canada Foreland Basin. *Sediment. Geol.* 385, 26–44.
- Horstwood, M.S., Košler, J., Gehrels, G., Jackson, S.E., McLean, N.M., Paton, C., Pearson, N.J., Sircombe, K., Sylvester, P., Vermeesch, P., Bowring, J.F., 2016. Community-derived standards for LA-ICP-MS U-(Th-) Pb geochronology—Uncertainty propagation, age interpretation and data reporting. *Geostand. Geoanal. Res.* 40 (3), 311–332.
- Hou, B., Keeling, J., Reid, A.J., Warland, I., Belousova, E., Frakes, L., Hocking, R., Fairclough, M., 2011. Heavy mineral sands in the Eucla Basin, Southern Australia: deposition and province-scale prospectivity. *Econ. Geol.* 106, 687–712.
- Hubbard, S., Leckie, D., Quinn, G.M., Daniels, B.G., Matthews, W., Guest, B., 2016. Accommodation, sediment provenance and paleo-drainage on the basal Cretaceous unconformity across the Canadian Western Interior Basin. In: Paper Presented at the American Association of Petroleum Geologists, Annual Convention and Exhibition, Calgary, AB, Program with Abstracts, June.
- Hubbard, S.M., Smith, D.G., Nielsen, H., Leckie, D.A., Fustic, M., Spencer, R.J., Bloom, L., 2011. Seismic geomorphology and sedimentology of a tidally influenced river deposit, Lower Cretaceous Athabasca oil sands, Alberta, Canada. *AAPG Bull.* 95 (7), 1123–1145.
- Jablonski, B.V., Dalrymple, R.W., 2016. Recognition of strong seasonality and climatic cyclicity in an ancient, fluvially dominated, tidally influenced point bar: Middle McMurray Formation, Lower Steepbank River, north-eastern Alberta, Canada. *Sedimentology* 63 (3), 552–585.
- Kjarsgaard, B., Harvey, S., Zonneveld, J., Heaman, L., White, D., MacNeil, D., 2006. Volcanic stratigraphy, eruptive sequences and emplacement of the 140/141 kimberlite, Fort `a la Corne field, Saskatchewan. In: Paper presented at the long abstracts, Kimberlite Emplacement Workshop, Saskatoon, Sask. <http://www.venuewest.com/8IKC/files/21%25%2020KjarsgaardHarvey.pdf> [accessed 18 June 2008].
- Knaust, D., 2017. *Atlas of Trace Fossils in Well Core: Appearance, Taxonomy and Interpretation*. Springer.
- La Croix, A.D., Dashtgard, S.E., 2014. Of sand and mud: sedimentological criteria for identifying the turbidity maximum zone in a tidally influenced river. *Sedimentology* 61 (7), 1961–1981.
- La Croix, A.D., Gingras, M.K., Dashtgard, S.E., Pemberton, S.G., 2012. Computer modeling bioturbation: the creation of porous and permeable fluid-flow pathways. *AAPG Bull.* 96 (3), 545–556.
- Leckie, D.A., Fustic, M., Seibel, C., 2009. Geoscience of one of the largest integrated SAGD operations in the world—a case study from Long Lake, northeastern Alberta. *Reservoir* 8.
- Lee, C.-T.A., Jiang, H., Ronay, E., Minisini, D., Stiles, J., Neal, M., 2018. Volcanic ash as a driver of enhanced organic carbon burial in the cretaceous. *Sci. Rep.* 8 (1), 4197.
- Ludwig, K., 2012. *Isoplot/Ex*, v. 3.75, 5. Berkeley Geochronology Center Special Publication, p. 75.
- Ludwig, K.R., 1998. On the treatment of concordant uranium-lead ages. *Geochim. Cosmochim. Acta* 62 (4), 665–676.

- Martin, H.K., 2018. Stratigraphic Characterization of an Early Cretaceous Channel-Belt Avulsion: Implications for Paleoenvironmental Interpretations of the McMurray Formation. Alberta, Graduate Studies.
- Matthews, W.A., Guest, B., 2017. A practical approach for collecting large-n detrital zircon U-Pb data sets by quadrupole LA-ICP-MS. *Geostand. Geoanal. Res.* 41 (2), 161–180.
- Melnyk, S., Gingras, M.K., 2020. Using ichnological relationships to interpret heterolithic fabrics in fluvio-tidal settings. *Sedimentology* 67 (2), 1069–1083.
- Miall, A.D., 1996. *The Geology of Fluvial Deposits*. Springer, Berlin, Heidelberg, New York (582pp.).
- Miller, J.R., Miller, S.M.O., 2007. *Contaminated Rivers: A Geomorphological-Geochemical Approach to Site Assessment and Remediation*. Springer Science & Business Media.
- Müller, G., Schöpfer, C., Vos, H., Kharazipour, A., Polle, A., 2009. FTIR-ATR spectroscopic analyses of changes in wood properties during particle and fibreboard production of hard- and softwood trees. *BioResources*, 4(1), 49–71.
- Musial, G., Reynaud, J.-Y., Gingras, M.K., Féliès, H., Labourdette, R., Parize, O., 2012. Subsurface and outcrop characterization of large tidally influenced point bars of the Cretaceous McMurray Formation (Alberta, Canada). *Sediment. Geol.* 279, 156–172.
- Muwais, W., Smith, D.G., 1990. Types of channel-fills interpreted from dipmeter logs in the McMurray Formation, northeast Alberta. *Bull. Can. Petrol. Geol.* 38 (1), 53–63.
- Nowell, A., Jumars, P., 1984. Flow environments of aquatic benthos. *Ann. Rev. Ecol. Syst.* 15 (1), 303–328.
- Paces, J.B., Miller Jr., J.D., 1993. Precise U-Pb ages of Duluth complex and related mafic intrusions, northeastern Minnesota: geochronological insights to physical, petrogenetic, paleomagnetic, and tectonomagmatic processes associated with the 1.1 Ga midcontinent rift system. *J. Geophys. Res.* 98 (B8), 13997–14013.
- Paton, C., Woodhead, J.D., Hellstrom, J.C., Hergt, J.M., Greig, A., Maas, R., 2010. Improved laser ablation U-Pb zircon geochronology through robust downhole fractionation correction. *Geochem. Geophys. Geosyst.* 11: Q 0AA06 (36 p.).
- Pemberton, S.G., Flach, P.D., Mossop, G.D., 1982. Trace fossils from the Athabasca oil sands, Alberta, Canada. *Science* 217 (4562), 825–827.
- Potter, P.E., 1955. The petrology and origin of the Lafayette Gravel: part 1. Mineralogy and petrology. *J. Geol.* 63 (1), 1–38.
- Ranger, M.J., Pemberton, S.G., 1992. The sedimentology and ichnology of estuarine point bars in the McMurray Formation of the Athabasca Oil Sands deposit, northeastern Alberta, Canada. In: Pemberton, S.G. (Ed.), *Applications of Ichnology to Petroleum Exploration*. Society of Economic Geologists and Paleontologists, Core Workshop 17, pp. 401–421.
- Ranger, M.J., Pemberton, S.G., 1997. Elements of a stratigraphic framework for the McMurray Formation in south Athabasca area, Alberta. In: Pemberton, S.G., James, D.P. (Eds.), *Petroleum Geology of the Cretaceous Manville Group, Western Canada*. Canadian Society of Petroleum Geologists Memoir 18, pp. 263–293.
- Reineck, H.-E., 1963. Sedimentgefüge im Bereich der südlichen Nordsee. *Abh. Senckenb. Naturforsch. Ges.* 505, 1–138.
- Reineck, H., Singh, I., 1980. *Depositional Sedimentary Environments*, 2nd edn. Springer-Verlag, Berlin.
- Rinke-Hardekopf, L., Dashtgard, S., MacEachern, J., 2019. Earliest cretaceous transgression of North America recorded in thick coals: McMurray Sub-Basin, Canada. *Int. J. Coal Geol.* 204, 18–33.
- Sabbatini, A., Negri, A., Bartolini, A., Morigi, C., Boudouma, O., Dinelli, E., Lurcock, P.C., 2016. Selective zircon accumulation in a new benthic foraminifer, *Psammophaga zirconia*, sp. nov. *Geobiology* 14 (4), 404–416.

- Sanford, L.P., 2008. Modeling a dynamically varying mixed sediment bed with erosion, deposition, bioturbation, consolidation, and armoring. *Comput. Geosci.* 34 (10), 1263–1283.
- Schäfer, W., 1956. Wirkungen der Benthos-Organismen auf den jungen Schichtverband. *Senckenb. Lethaea* 37, 183–263.
- Schneider, A.B., Koschinsky, A., Kiprotich, J., Poehle, S., do Nascimento, P.C., 2016. An experimental study on the mixing behavior of Ti, Zr, V and Mo in the Elbe, Rhine and Weser estuaries. *Estuar. Coast. Shelf Sci.* 170, 34–44.
- Seilacher, A., 1967. Bathymetry of trace fossils. *Mar. Geol.* 5 (5–6), 413–428.
- Shchepetkina, A., Speta, M., Gingras, M.K., Rivard, B., Pemberton, S.G., 2017. Hyperspectral imaging as an aid for facies analysis in massive-appearing sediments: a case study from the middle McMurray Formation. *Bull. Can. Petrol. Geol.* 65 (2), 262–278.
- Smith, D.G., 1989. Comparative sedimentology of mesotidal (2 to 4 m) estuarine channel point-bar deposits from modern examples and ancient Athabasca oil sands (Lower Cretaceous), McMurray Formation. In: Reinson, E. (Ed.), *G. Canadian Society of Petroleum Geologists, Modern and ancient examples of clastic tidal deposits – A core and peel workshop*, pp. 60–65.
- Smith, D.G., Hubbard, S.M., Leckie, D.A., Fustic, M., 2009. Counter point bar deposits: lithofacies and reservoir significance in the meandering modern Peace River and ancient McMurray Formation, Alberta, Canada. *Sedimentology* 56 (6), 1655–1669.
- Spila, M. V., Pemberton, S. G., Rostron, B., Gingras, M. K., 2009. Biogenic textural heterogeneity, fluid flow and hydrocarbon production: Bioturbated facies Ben Nevis Formation, Hibernia field, offshore Newfoundland. In: MacEachern, J.A., Bann, K.L., Gingras, M.K., Pemberton, S.G. (Eds.), *Applied Ichnology*, SEPM Short Course Notes 52, pp. 363–380.
- Taylor, A., Goldring, R., 1993. Description and analysis of bioturbation and ichnofabric. *J. Geol. Soc. London* 150, 141–148.
- Thomas, R.G., Smith, D.G., Wood, J.M., Visser, J., Calverley-Range, E.A., Koster, E.H., 1987. Inclined heterolithic stratification – terminology, description, interpretation and significance. *Sediment. Geol.* 53 (1–2), 123–179.
- Tonkin, N.S., McIlroy, D., Meyer, R., Moore-Turpin, A., 2010. Bioturbation influence on reservoir quality: a case study from the Cretaceous Ben Nevis Formation, Jeanne d’Arc Basin, offshore Newfoundland, Canada. *AAPG Bull.* 94 (7), 1059–1078.
- Tourtelot, H.A., 1968. Hydraulic equivalence of grains of quartz and heavier minerals and implications for the study of placers. *US Geol Survey Prof. Pap.* 594-F. Government Printing Office, p. 13.
- Trevena, A.S., Nash, W., 1981. An electron microprobe study of detrital feldspar. *J. Sediment. Res.* 51 (1), 137–150.
- Vogel, S., 1994. *Life in Moving Fluids: The Physical Biology of Flow*. Princeton University Press.
- von Rad, U., 1972. Zur Sedimentologie und Fazies des Allgäuer Flysches. *Geol. Bavarica* 66, 92–147.
- Wetzel, A., 2008. Recent bioturbation in the deep South China Sea: a uniformitarian ichnologic approach. *Palaios* 23, 601–615.
- Wetzel, A., 2009. The preservation potential of ash layers in the deep-sea: the example of the 1991-Pinatubo ash in the South China Sea. *Sedimentology* 56 (7), 1992–2009.
- Wetzel, A., Szczygielski, A., Unverricht, D., Stattegger, K., 2017. Sedimentological and ichnological implications of rapid Holocene flooding of a gently sloping mud-dominated incised valley – an example from the Red River (Gulf of Tonkin). *Sedimentology* 64, 1173–1202.
- White, D., Kjarsgaard, B., Mwenifumbo, C., Buffett, G., 2007. Seismic delineation of the Orion South (140/141) kimberlite Fort a la Corne Field, Saskatchewan. In: *Exploration 07: Fifth Decennial International Conference on Mineral Exploration*; Toronto; CA; September 9–12, 2007.
- Wightman, D.M., Pemberton, S.G., 1997. The Lower Cretaceous (Aptian) McMurray Formation: an overview of the Fort McMurray area, northeastern, Alberta.